Urban Climate 68 (2026) 103052

Contents lists available at ScienceDirect

Urban Climate

journal homepage: www.elsevier.com/locate/uclim

Downscaling extreme winds to the building scale for resilient critical infrastructure

Petros Ampatzidis [a,b,*], Carlo Cintolesi [a], Francesco De Martin [a], Andrea Petronio [c], Andrea Zonato [d], Silvana Di Sabatino [a]

[a] Group of Atmospheric Physics, Department of Physics and Astronomy "Augusto Righi", University of Bologna, via Irnerio 46, Bologna, 40126, Italy
[b] Centre for Climate Adaptation & Environment Research, Dept of Architecture and Civil Engineering, University of Bath, Claverton Down, Bath, BA2 7AY, UK
[c] National Institute of Oceanography and Applied Geophysics - OGS, Via Beirut 2, Trieste, 34151, Italy
[d] CIMA Research Foundation, Savona, Italy

ARTICLE INFO

Keywords:
Multiscale simulations
Extreme wind events
Numerical downscaling
Atmospheric load
WRF
OpenFOAM

ABSTRACT

Extreme winds pose a growing threat to critical infrastructure under climate change; yet their impact at building scale remains poorly quantified because conventional atmospheric modelling approaches do not adequately represent small-scale processes. Here, we develop and apply a downscaling numerical methodology that transfers mesoscale atmospheric information to the building scale, enabling a physically consistent assessment of the impact of extreme winds. We examine a representative high-rise hospital situated in complex terrain and regularly exposed to severe windstorms (Bora). The wind dynamics and resulting loads are reproduced numerically, first by employing the idealised logarithmic boundary layer model for the incoming flow and subsequently by downscaling realistic outputs from a mesoscale meteorological model. The mesoscale-informed simulations capture terrain-induced wind structures, including upstream recirculation regions and a distinct low-level jet, which are not captured by the logarithmic approach. Incorporating mesoscale vertical velocity redistributes momentum and turbulence across height, increasing turbulent kinetic energy near the ground while reducing pressure coefficients along the windward façade. In contrast, simulations based on idealised inflow conditions underestimate both turbulence levels and windward pressure loads. It is shown, for the first time for severe windstorms, that considering realistic atmospheric conditions is key to more accurately reproducing wind dynamics and atmospheric load at building scale, and flow dynamics must be carefully represented in downscaling approaches to avoid biased results. Our findings support the incorporation of mesoscale information into engineering assessments of critical infrastructure exposed to extreme winds, thereby strengthening the physical basis upon which risk and resilience analyses are conducted.

1. Introduction

Extreme weather events have emerged as one of the most significant global challenges of the 21st century (UN, 2020). In the context of a changing climate, extreme weather and climate events pose, and will continue to pose, a substantial threat to human

* Corresponding author at: Centre for Climate Adaptation & Environment Research, Dept of Architecture and Civil Engineering, University of Bath, Claverton Down, Bath, BA2 7AY, UK.
E-mail address: p.ampatzidis@bath.ac.uk (P. Ampatzidis).

https://doi.org/10.1016/j.uclim.2026.103052
Received 12 January 2026; Received in revised form 5 June 2026; Accepted 10 July 2026
Available online 17 July 2026
2212-0955/© 2026 The Authors. Published by Elsevier B.V. This is an open access article under the CC BY license (http://creativecommons.org/licenses/by/4.0/).

lives, ecosystems, and economies. Among these, extreme wind events, such as storms, tropical and extratropical cyclones, have increased in frequency by about 40% over the past two decades compared with the period 1980–1999 (UN, 2020). The impact of extreme winds on the urban environment is twofold: they endanger pedestrian safety and activity, and cause damage or loss of functionality in critical infrastructure systems (Repetto et al., 2018; Pastori and Mazzucchelli, 2023; Avolio et al., 2026). Tall buildings are particularly susceptible to wind-induced damage, with significant economic consequences arising both from direct structural losses and from the interruption of business activities (Metwally et al., 2025). Among them, hospitals represent a critical subset, as their loss of functionality during or after an extreme wind event can severely hinder healthcare delivery and amplify cascading socioeconomic impacts across entire regions. Nevertheless, progress in assessing the risks associated with extreme wind events and in adapting critical assets to climate change remains at an early stage (EC, 2021; Leal Filho et al., 2024).

An accurate assessment of structural risks at the building scale depends on accurately reproducing local atmospheric conditions and the urban boundary layer (Potsis et al., 2023). Mesoscale weather systems greatly affect urban atmospheric dynamics, modulating wind speed, direction, and turbulence characteristics across the urban boundary layer. State-of-the-art weather models provide useful information at regional and global scales, but do not adequately represent urban-scale phenomena in detail (Garuma, 2018; Nogueira et al., 2020). Realistic wind estimation at the building scale is complex and challenging, further complicated when extreme winds interact with complex topography, where the orography strongly affects the flow. This is because accurate numerical modelling of terrain topography, urban morphology, and reproduction of atmospheric dynamics and turbulence are required, all of which play a key role in the estimation of wind impacts (Dagnew and Bitsuamlak, 2013). Accurately resolving these interacting processes requires a multiscale modelling framework in which atmospheric information is progressively downscaled from mesoscale to building-scale simulations.

Mesoscale numerical weather prediction (NWP) dynamically downscale atmospheric data and reproduce the influence of terrain and surface heterogeneity at kilometre-scale resolutions (Dudhia, 2014). Traditionally, the buildings in these models are represented by roughness lengths or parametrised by urban canopy models (Jandaghian and Berardi, 2020). Computational Fluid Dynamics (CFD) models have been proven to be a valuable tool for studying the wind velocity and pressure fields around buildings, providing information for the entire flow field and all relevant variables (Blocken, 2014; Toparlar et al., 2017), but also to simulate extreme meteorological events (Cintolesi et al., 2026). In contrast to mesoscale NWP models, the ability of CFD models to directly resolve the roughness sublayer, i.e. the atmospheric layer between the ground and about two to five times the building height, and the urban canopy layer, i.e. the layer extending from the ground to the roof level where most human activities take place, has made them indispensable for urban physics studies (Oke et al., 2017).

The incorporation of mesoscale meteorological data into building-scale simulation has been explored in the past two decades (Yamada and Koike, 2011), demonstrating its advantages in capturing wind circulation patterns with greater accuracy compared to stand-alone CFD models in urban environments. Although there is still a lack of best-practice guidelines and standard procedures for transferring mesoscale information at the microscale (Ricci et al., 2022), such methodologies have been applied in various contexts, including the dispersion of pollutants (Tewari et al., 2010; Miao et al., 2013; Zheng et al., 2015), wind resource assessment (Durán et al., 2020; Castorrini et al., 2021, 2023), and the evaluation of pedestrian-level wind comfort (Huang et al., 2023). In addition, few studies have used meso-microscale coupling to assess wind dynamics in complex terrains, where orographic influences can generate spatially variable flow structures, including gust fronts, vertical motions, channelled flows, and local recirculation areas (Fernando, 2010; Bilal et al., 2016; Castorrini et al., 2021; Yue et al., 2024; He et al., 2025). Despite the valuable insights provided by the existing range of studies, there is a clear gap in accounting for the influence of mesoscale meteorological systems under extreme weather conditions.

Extreme wind events, although often short-lived and localised, can produce peak wind loads and complex wind and turbulence structures that cannot be accurately captured by ad hoc boundary-layer models that are typically used as inflow conditions in building-scale studies, such as the logarithmic wind profile (Richards and Hoxey, 1993; Richards and Norris, 2011). Recently, some effort has been made to leverage meteorological information to study the flow field, wind load, and hazards that occur around buildings during an extreme wind event. Zhao et al. (2023) and Huang et al. (2024) coupled the Weather Research and Forecasting (WRF) model with Reynolds-Averaged Navier–Stokes (RANS) and Large-Eddy Simulation (LES) models, respectively, to assess the impact of typhoons on pedestrian-level wind environment and wind-induced vibrations on tall buildings in Hong Kong, while Kim et al. (2025) incorporated meteorological fields of a typhoon in South Korea into the Parallelised Large-Eddy Simulation Model (PALM) appraising the effects of building height on pedestrian-level wind. For a typhoon in Shanghai, Yang et al. (2025) coupled WRF with PALM to simulate an urban neighbourhood under extreme wind, showcasing that building area fraction is strongly correlated with pedestrian distress. Together, these studies indicate that most of the existing literature has focused on tropical cyclones, particularly typhoons, which are among the most common extreme wind events in East and Southeast Asia. However, there is a clear gap in studies that assess the impact of other types of extreme wind on urban areas, such as downslope windstorms, which are typical in areas located on the lee side of mountains. In addition, little attention has been given to how mesoscale vertical velocities influence building-scale predictions of wind loading and turbulence, even though such vertical motions are a defining feature of many storm systems.

One of the most characteristic windstorms in Europe is the Bora, a gusty northeasterly wind that blows along the eastern coast of the Adriatic Sea and that frequently reaches hurricane strength, with hourly mean wind speeds exceeding 20 m/s and gusts up to 70 m/s (Belušić et al., 2007; Boldrin et al., 2009; Grisogono and Belušić, 2009; Beg Paklar et al., 2001). The Bora is characterised by strong low-level jets and mountain-wave breaking that often leads to hydraulic jumps, generating intense shear layers, flow separation, recirculation regions, and highly heterogeneous near-ground wind fields. Similar windstorms are observed in other mountainous areas worldwide, e.g. the Front Range of the Rocky Mountains and the western slopes of the Andes (Grisogono and

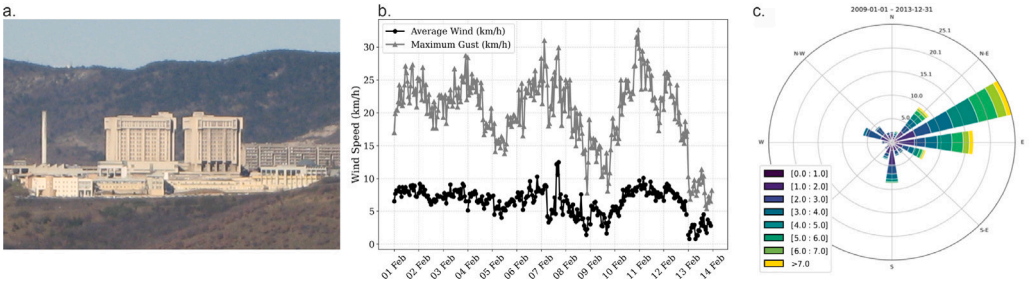

Fig. 1. (a) An overview of the Cattinara hospital located downwind of the Karst Plateau from where the Bora wind usually blows. (b) Average wind speed and maximum gusts during the extreme Bora wind event in February 2012, as measured upwind of the hospital at an elevation of about 5 m above ground. (c) Wind rose for a 5-year period 2009–2013.

Belušić, 2009). These phenomena share key physical mechanisms: strong pressure gradients, mountain-wave breaking, and turbulent downslope jets. The Adriatic Bora, however, represents an ideal case for studying these processes due to its proximity to urbanised coastal regions and its extensive observational record, spanning more than a century (Mohorovičić, 1889). Previous studies have examined its seasonality and gust statistics (Enger and Grisogono, 1998; Heimann, 2001), driving mechanisms (Klemp and Durran, 1987; Smith, 1987), and mesoscale structure (Večenaj et al., 2010; Davolio et al., 2015; Belušić Vozila et al., 2024). Microscale investigations have focused on near-surface velocity profiles and turbulent fluxes (Lepri et al., 2014; Babić et al., 2016; Wang et al., 2025), their effects on vehicles and wind barriers (Kozmar et al., 2012b,a), and the influence of orography on turbulent dynamics (Golem and Večenaj, 2023). However, the impact of such windstorms on single buildings, particularly critical assets such as hospitals, remains largely unexplored. Key questions remain: how do windstorms, through their interaction with complex topography, modify the local flow field around structures, and what are the resulting wind loads on critical infrastructure? Addressing these questions is crucial for improving predictive capabilities and enhancing resilience as extreme weather events intensify under climate change (Seneviratne et al., 2021).

In this study, a multiscale numerical methodology is introduced to downscale mesoscale meteorological data from an extreme wind event to the building scale. The novelty of this work lies in the application of a WRF-OpenFOAM modelling approach to a severe Bora windstorm affecting a high-rise hospital building in complex terrain, demonstrating for the first time how mesoscale atmospheric structures associated with a Bora event can propagate to the building scale and influence local flow patterns, turbulence characteristics, and aerodynamic loading. The proposed methodology is generalisable to other extreme wind types and geographic contexts, offering a systematic pathway for integrating mesoscale atmospheric dynamics into building-scale engineering assessments, thereby strengthening the physical basis upon which risk and resilience analyses are conducted. Specifically, the objectives are to: (a) develop and apply a downscaling methodology that enables the use of mesoscale meteorological data in microscale numerical modelling, (b) evaluate its performance against conventional approaches that employ idealised logarithmic inflow profiles, and (c) quantify the influence of realistic extreme wind conditions on flow behaviour and atmospheric loading.

2. Problem definition and simulation approach

2.1. Case study description

Trieste is a coastal city in northeastern Italy located between the Adriatic Sea and the Karst Plateau, where Bora winds are strongly influenced by the complex terrain. The study focuses on the Cattinara Hospital complex, located on an elevated site on the outskirts of the city and comprising several high-rise buildings, including two 54 m twin towers (Fig. 1a). Owing to its exposure to severe Bora winds and its role as critical healthcare infrastructure, the hospital is a relevant case study for assessing the impacts of extreme winds on complex urban environments.

According to previous studies (Beg Paklar et al., 2001; Dorman et al., 2006; Alpers et al., 2009; Boldrin et al., 2009; Raicich et al., 2013; Davolio et al., 2015) and historical records from three local weather stations operated by the Environmental Agency of the Friuli-Venezia Giulia region (ARPA FVG), the most severe Bora wind event of the past 35 years occurred in February 2012. During this 12-day episode, wind speeds in Trieste reached up to 47 m/s (170 km/h). Fig. 1b presents the hourly wind speed and maximum gusts measured during the event upwind of the Cattinara hospital at about 5 m above ground, highlighting that the peak intensities occurred on 10–11 February. These two days are selected as the reference period for subsequent numerical simulations, representing the most extreme and sustained Bora conditions observed in recent decades. The 5-year wind rose (2009–2013) reported in Fig. 1c confirms the Bora as the dominant wind in the region, occurring approximately 25% of the time and predominantly blowing from the east-northeast (67.5°). Accordingly, the present study focuses on the dominant E–NE Bora sector associated with the analysed extreme event, as this represents the prevailing wind affecting the hospital site.

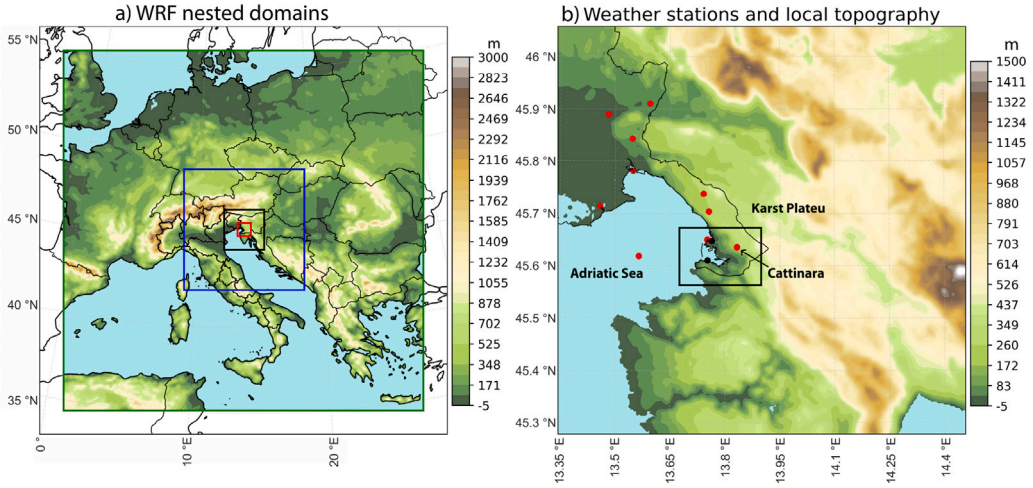

Fig. 2. (a) The four nested domains of the mesoscale simulation. *d*01: green, 9 km horizontal resolution, *d*02: blue, 3 km horizontal resolution, *d*03: black, 1 km horizontal resolution, *d*04: red, 333 m horizontal resolution. (b) Terrain orography and location of local weather stations in the innermost *d*03 domain. Weather stations depicted in black only record temperature and relative humidity.

2.2. Multiscale numerical methodology

The methodology to effectively downscale mesoscale weather information of an extreme Bora wind event, to provide realistic boundary conditions for subsequent building-scale simulations, consists of three main steps: (a) ERA5 reanalysis data – the state of the art in terms of the representation of the climate of the past (Hersbach et al., 2020) – are collected for the duration of the particularly severe 2012 Bora wind event. These data come with a horizontal resolution of about 25 km at mid-latitudes, and are thus not suitable for passing information down to the building scale (resolution of 1 m); (b) The WRF model 4.5.1 (Skamarock et al., 2019) is used to dynamically downscale the ERA5 data to a horizontal resolution of 333 m. Initialisation profiles are extracted from WRF simulations upwind of the inlet boundary of the CFD computational domain; (c) These profiles are then used as inflow conditions for a series of RANS simulations around the Cattinara hospital. It should be noted that although a historical extreme wind event is downscaled here, the same approach can be expanded to a climate perspective, i.e applying the same methodology to climatic projections downscaled using WRF.

It is worth noting here a few words about the non-logarithmic profile of the Bora wind that is passed on for RANS simulations. The RANS model reproduces numerically the wind dynamics by resolving the primitive equations of motion, avoiding use of empirical parametrisation and case-specific settings. Hence, the model needs only averaged dynamical quantities as boundary conditions, subsequently developing the local physical processes and wind dynamics on the basis of the local topography and urban morphology. Because of this generality of the small-scale model, RANS has no issues with consistency or agreement with a non-logarithmic inflow profile. Information regarding mesoscale dynamics is taken into account by WRF and incorporated into the simulation via the boundary conditions.

2.3. Mesoscale simulations setup

The selected Bora event occurred during February 2012 under strong synoptic-scale pressure gradients between central Europe and the Adriatic region, generating persistent E-NE downslope flow over the Karst Plateau and the Gulf of Trieste.

The WRF simulations are initialised at midnight on 10 February 2012 using the 38 vertical levels of ERA5, and are carried out with 64 vertical levels, the lowest of which is approximately 5 m above ground level (AGL). The same model configuration was recently used to simulate a convective windstorm in the city of Milan, Italy (De Martin et al., 2025). The sensitivity to the choice of the lowest model level is assessed by comparing with a higher vertical level of 10 m AGL (as seen in Table A.1).

Four one-way nested simulations are carried out to dynamically downscale the ERA5 data to a sub-km resolution, with a grid spacing of 9 km, 3 km, 1 km and 333 m, respectively, and 300 × 300 grid points each (Fig. 2a). The orientation of the simulation domains is slightly shifted eastward with respect to the Cattinara hospital, as the Bora wind predominantly blows from east-northeast, to allow WRF to accurately reproduce the wind dynamics (Fig. 2b). The Planetary Boundary Layer (PBL) is parametrised with the Mellor–Yamada–Yanjic scheme (MYJ, Mellor and Yamada, 1982; Janjić, 1994); the Thompson scheme is used for microphysics processes (Thompson et al., 2008); the rapid radiative transfer model (RRTM, Mlawer et al., 1997) is used for long-wave radiation and the Dudhia scheme (Dudhia, 1989) for short-wave radiation; Noah is used as the land surface model (Mukul Tewari et al., 2004). The setup of the physical parametrisation suite is chosen based on the performance of different model configurations against data from 11 ground weather stations obtained from ARPA FVG (Fig. 2b) for 10 and 11 February 2012. The validation procedure is shown in Appendix.

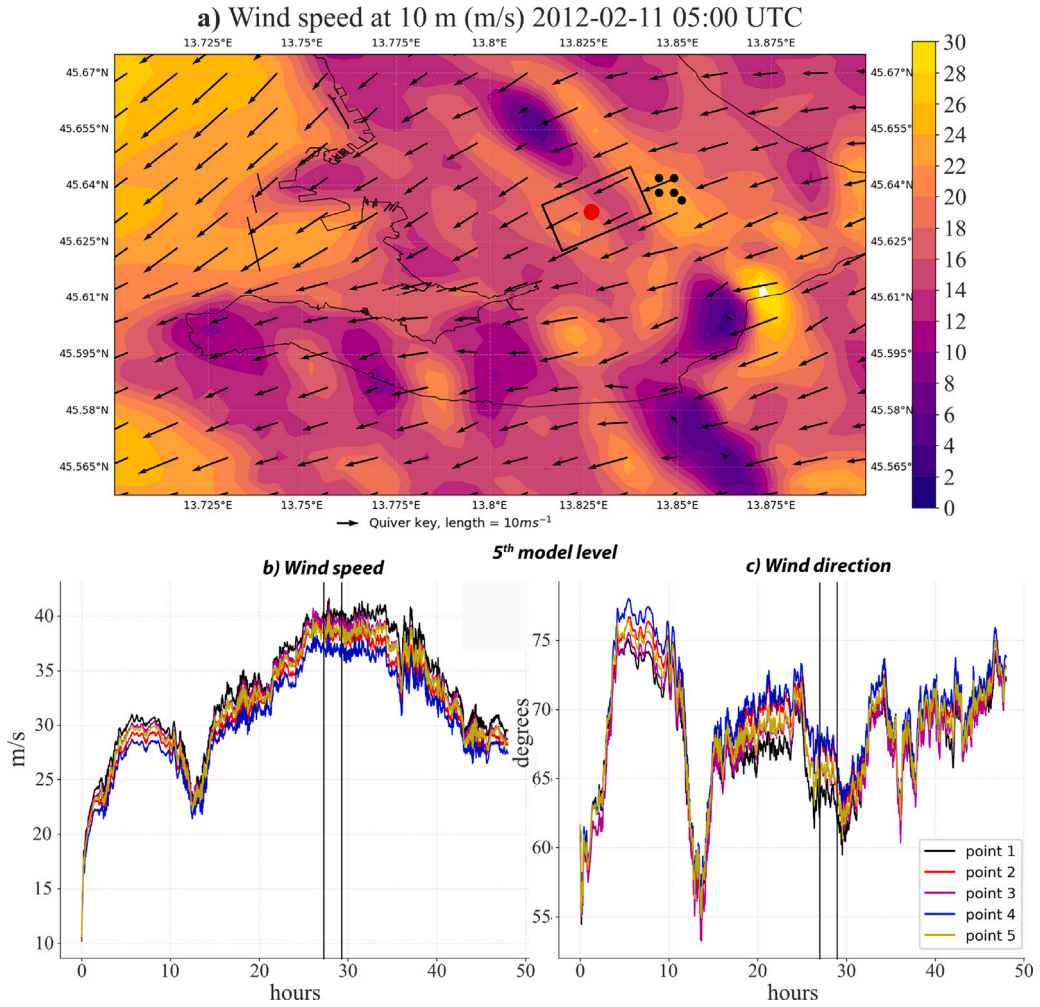

Fig. 3. (a) Wind field in the innermost *d*04 domain (see 2b) at 05:00 on 11 February 2012. The black box denotes the CFD domain, the red dot the location of the Cattinara hospital, whilst the black dots show the location of the five grid points used to initialise the CFD simulation. (b) Time series of wind speed throughout the simulation for the innermost *d*04 domain, with 0 being the start of the simulation at 00:00 on 10 February 2012. The vertical lines highlight the averaging period for the generation of the initialisation profiles for the subsequent CFD simulations. (c) Same as (b) but for the wind direction.

2.4. Inflow profiles for building-scale simulations

For the generation of a realistic inflow conditions representative of the Bora flow approaching the CFD domain, five neighbouring grid points are sampled in the innermost domain *d*04 on the relatively flat Karst Plateau upstream of the hospital site (Fig. 3a). The use of multiple points allows a more spatially representative characterisation of the incoming mesoscale flow. The time evolution of the wind speed and direction in these five points is studied to select the peak intensity of the Bora, as well as a period of almost stationarity of the flow in order to avoid transition phases. A two-hour window, between 03:00 and 05:00 on 11 February 2012, is selected (Fig. 3b, c). For each selected grid point, vertical profiles of velocity and turbulence quantities are extracted from the WRF simulations over the selected two-hour period. These profiles are subsequently averaged both temporally and spatially across the five points to generate representative inlet profiles for the CFD simulations.

It should be noted here that although the Bora wind is characterised by strong turbulence and intermittent gusts, it is known to be associated with sustained synoptic forcing and persistent downslope flow structures that can remain relatively stationary over several hours (Belušić Vozila et al., 2024; Grisogono and Belušić, 2009). The present study therefore focuses on reproducing the quasi-stationary mean atmospheric structure of a Bora event, which coincides with its peak phase, rather than its instantaneous gust dynamics.

Some features of the computed inlet wind profile need further attention. The CFD simulations require a vertical profile of turbulent kinetic energy (TKE) as an input variable. From a mesoscale point of view, the TKE is the sum of the resolved (TKE_{RES})

and parametrised part (TKE_{PAR}) by the turbulence scheme. TKE_{RES} is calculated directly from the model output, for each time step, and then averaged temporally over 20 min, as in Zonato et al. (2022). It is computed as $TKE_{RES} = \frac{1}{2}\overline{u_i' u_i'}$, where u_i are the velocity components ($i = 1, 2, 3$), the overbar denotes the 20-minute time average, and the velocity fluctuation is computed as $u_i' = u_i - \overline{u_i}$.

TKE_{PAR} is calculated by the MYJ scheme, using a 1.5-order closure (Mellor and Yamada, 1982):

$$\frac{D\,TKE_{PAR}}{Dt} = \frac{\partial}{\partial z}\left[S\ell\sqrt{2\,TKE_{PAR}}\frac{\partial TKE_{PAR}}{\partial z}\right] - \overline{w'u'}\frac{\partial U}{\partial z} - \overline{w'v'}\frac{\partial V}{\partial z} + \frac{g}{\theta}\overline{w'\theta'} - \varepsilon. \tag{1}$$

where ℓ is the diagnostic mixing length scale, S is a dimensionless constant equal to 0.2, $\overline{w'u'}$ and $\overline{w'v'}$ are the parametrised mechanical production terms, $\overline{w'\theta'}$ is the parametrised thermal production, U and V are the mean horizontal wind components of the flow, g is gravitational acceleration and θ is the potential temperature. Lastly, ε is the turbulent dissipation coefficient computed as:

$$\varepsilon = \frac{TKE_{PAR}^{3/2}}{B_1\,\ell}, \tag{2}$$

where $B_1 \approx 1.878$ is a dimensionless closure constant.

2.5. Building-scale simulations

The mesoscale simulations described in the previous sections provide realistic inflow conditions for the extreme wind event but do not explicitly capture flow interactions with individual buildings. A higher-resolution CFD model resolving the urban geometry is adopted to investigate the flow at the building scale.

2.5.1. Mathematical model and numerical approach

The ambient fluid is dry air, modelled as an incompressible, viscous Newtonian fluid. The flow is governed by the incompressible Navier–Stokes equations:

$$\frac{\partial u_j}{\partial x_j} = 0, \tag{3}$$

$$\frac{\partial u_i}{\partial t} + u_j\frac{\partial u_i}{\partial x_j} = -\frac{1}{\rho_0}\frac{\partial p}{\partial x_i} + \nu\frac{\partial^2 u_i}{\partial x_j x_j}, \tag{4}$$

where u_i is the velocity component (m/s) in the x_i direction, p is pressure (Pa), ρ_0 is the reference density of the dry air (kg/m^3) and ν is the kinematic viscosity (m^2/s).

The simulations employ a RANS approach to describe the stationary flow by averaging in time the equations of motion (Pope, 2013). The standard $k-\varepsilon$ turbulence model is employed to simulate the turbulent characteristics of the flow and close the system (Launder and Spalding, 1974). Such a model is well-suited for capturing the effects of turbulent viscosity and dissipation of kinetic energy in complex airflow scenarios, and it has been widely employed for aerodynamic simulations around buildings. For the sake of conciseness, its formulation is not reported here.

The simulations are performed using the open-source code OpenFOAM (ESI-OpenCFD, 2020), adapting the model described in Ampatzidis et al. (2022, 2024). This model has been extensively validated against wind tunnel experiments and shown to accurately reproduce steady-state atmospheric flow fields around single- and multi-building configurations. As the present work adopts the same CFD modelling approach, additional validation is not repeated here. All spatial discretisation schemes are second-order accurate; central differencing is employed for the velocity field, while bounded second-order schemes are used for the turbulent kinetic energy and dissipation rate to ensure numerical stability. Convergence is assessed by monitoring residuals and by tracking the temporal evolution of velocity at selected probe locations within the domain.

2.5.2. Computational domain

The computational mesh integrates topographic and building morphology data. Geographic data is provided by the Friuli-Venezia Giulia Region Geographic Resource System and pre-processed with QGIS (QGIS Development Team, 2024). The terrain data are converted to a stereolithography file format with an overall resolution of 1 m near the building structure, and all buildings are georeferenced. Smoothing techniques are applied to the terrain data to facilitate meshing.

The computational domain is designed to encompass significant topological features. It is orientated towards the E-NE direction as per the dominant Bora wind direction. The domain boundaries are set up following existing guidelines (Franke et al., 2007; Tominaga et al., 2008; Blocken, 2015). The area of interest (AoI) encompasses the buildings that comprise the hospital complex. The inlet boundary is placed at 1100 m upwind of the AoI – almost 20 times the hospital height (H=54 m) – ensuring coverage of the Karst plateau, a relatively flat region, from where the Bora winds blow. Had the inlet boundary been placed at a closer distance, i.e. where the terrain elevation changes and the slope begins, it could have introduced artificial acceleration effects at the domain entrance, distorted turbulence structures, and numerical instabilities in the simulated flow field. The selected inlet location, therefore, ensures that the incoming Bora flow develops naturally over a relatively flat terrain before reaching the downslope. Similarly, the outlet boundary is placed 700 m from the AoI ($> 10H$) with an additional 200 m buffer to allow flow development and minimise the impact of the outlet boundary on the AoI. The lateral boundaries are placed 600 m from the AoI with an additional 300 m buffer on both sides to ensure minimal impact and a blockage ratio lower than 3% (Blocken, 2015). The domain extends vertically

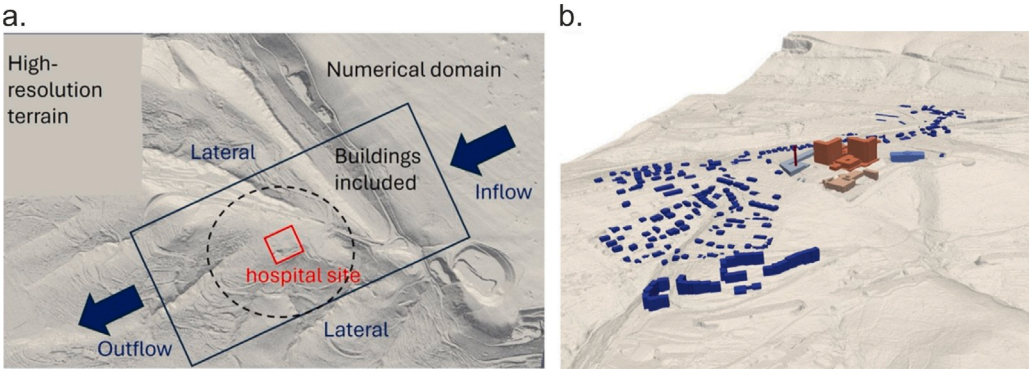

Fig. 4. (a) An overview of the generated complex terrain, the AoI (in red), and the outline and orientation of the computational domain. (b) A geometrical representation of the explicitly modelled buildings, including the Cattinara hospital in orange.

to 850 m ($> 15H$), a height necessary to capture the complex flow dynamics above the terrain and buildings, and to accommodate the significant elevation changes—about 220 m from inlet to outlet.

According to Franke et al. (2007), a building with height H_n has minimal influence on flow dynamics within the AoI if the distance from it is greater than $10H_n$. More recent studies have come up with new suggestions: Liu et al. (2018) propose to include buildings within a radius of three times the maximum dimension of the target building, while Zheng et al. (2021) introduced a more comprehensive approach estimating the surrounding region depending on the target building height and building density. For this study, the former gives a radius of 465 m, as the length of the main hospital complex is approximately 155 m, while according to the latter method and with a local building density of 20%, the estimated radius comes to $9H = 486$ m. Therefore, all buildings within a radius of 500 m are explicitly modelled. Nonetheless, as those suggestions mostly refer to cases with a flat ground surface, we have chosen to adopt a more conservative radius of 850 m ($> 15H$) to account for the impact of terrain-induced flow modification and potential upstream building interactions under the Bora flow. In this expanded radius, though, we have not explicitly modelled buildings located at considerably lower elevations relative to the hospital, particularly those outside the primary Bora flow sector and separated by terrain shielding, as their aerodynamic influence on the local flow field around the hospital is expected to be negligible compared with the dominant terrain-driven Bora structures. An overview of the generated complex terrain and the computational domain with respect to the local topography is presented in Fig. 4.

2.5.3. Case studies and boundary conditions

To appraise the impact of inflow conditions on the flow structure and atmospheric load on the Cattinara Hospital under the dominant E–NE Bora wind direction associated with the selected extreme event, two cases are considered: (a) a case using idealised logarithmic profiles for atmospheric flows, and (b) a case using realistic profiles derived from the downscaled mesoscale simulations. To ensure comparability between the two cases, the idealised profiles are generated using the velocity and height of the first cell of the realistic case as the reference velocity and the reference height, respectively. Consequently, the two cases differ only in their inflow profiles for velocity, TKE, and dissipation rate. The inflow profiles for the mesoscale-informed case are detailed in Section 3.2.

The idealised inflow profiles for velocity, TKE, and dissipation rate are those proposed by Richards and Hoxey (1993) and later revisited by Richards and Norris (2011) for a neutral atmospheric boundary layer:

$$U(z) = \frac{u^*_{ABL}}{\kappa} \ln\left(\frac{z + z_0}{z_0}\right), \quad k(z) = \frac{{u^*_{ABL}}^2}{\sqrt{C_\mu}}, \quad \varepsilon(z) = \frac{{u^*_{ABL}}^3}{\kappa(z + z_0)}, \tag{5}$$

where z is the vertical direction, $z_0 = 0.5$ m is the aerodynamic roughness length, u^*_{ABL} the friction velocity, $C_\mu = 0.09$ is a model constant, and $\kappa = 0.4$ is the von Kármán constant. The friction velocity is estimated at $u^*_{ABL} = 1.8$ m/s, based on the velocity and height of the first vertical cell of the WRF simulations as noted above.

The buildings and ground are modelled as adiabatic while thermal effects are neglected in the simulations. Our assumption is that during the extreme Bora wind by the focus on a particularly extreme wind event during winter time where the wind dynamics and wind-induced loads are dominated by mechanical forcing rather than by thermal stratification or surface heating effects. Although this approach excludes the representation of thermal processes, it is consistent with the aim of isolating the dynamical impact of strong winds on the urban flow field and on the resulting loads acting on the hospital structures. At the start of the simulations, the air is assumed to be at rest, ensuring that the development of the flow is driven entirely by the imposed inlet conditions. The Reynolds number for all cases, calculated using the characteristic length of the average height of the inlet boundary ($L_{ref} = 511$ m), is approximately 1.7×10^9, placing the flow within the turbulent regime.

Initial conditions for TKE and ε are estimated using a specified turbulent intensity I and the Prandtl mixing length l_m:

$$k_{in} = \frac{3}{2}(|u|I)^2, \quad \varepsilon_{in} = C_\mu^{3/4} \frac{k^{3/2}}{l_m}, \tag{6}$$

Table 1
An overview of the simulated CFD cases with a brief description of their inflow conditions.

Case	U	W	TKE	ε
Log	Eq. (5)	None	Eq. (5)	Eq. (5)
WRF-U	WRF-informed	None	WRF-informed	WRF-informed
WRF-UW	WRF-informed	WRF-informed	WRF-informed	WRF-informed

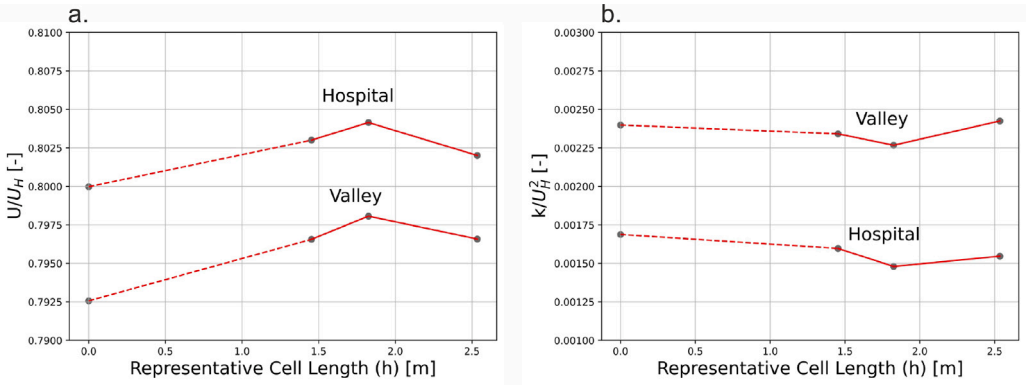

Fig. 5. Results of the grid independence study for (a) normalised velocity and (b) normalised turbulent kinetic energy values at the location of the Cattinara hospital and in the valley upstream of the area of interest.

where $|u|$ is the free-stream flow speed. For an accurate estimation of l_m and I, the upstream flow conditions must be known. For external flows of medium to low intensity, I can be estimated using a power-law function of the Reynolds number Re as $I = 0.055\,Re^{-0.041}$. For wall-bounded flows, with a boundary layer thickness δ, the mixing length can be estimated as $l_m = 0.4\delta$, where δ can be, in turn, estimated from the analytical solution of $\delta/x \approx 0.37\,Re^{-1/5}$, where x is a characteristic length in the x-direction. More details can be found in Greenshields and Weller (2022).

At the outlet, a mixed zero-gradient and Dirichlet boundary condition (*inletOutlet*), based on the flux direction, is set for all variables except pressure, for which a uniform fixed value of zero is applied. At the top and lateral boundaries, slip conditions are used for all variables, as those boundaries are placed sufficiently far from the AoI. At the walls, wall functions for atmospheric boundary layer flows are used: *atmNutkWallFunction* for the turbulent viscosity—applied to the rough ground away from the AoI; *nutkWallFunction* for the turbulent viscosity on the explicitly modelled buildings and ground within the AoI (Blocken et al., 2007); *atmEpsilonWallFunction* for ε and *kqRWallFunction* for TKE. The aerodynamic roughness length of the terrain is set to $z_0 = 0.5$, taken as representative of the complex terrain and vegetation cover in the vicinity of the inlet (Wieringa, 1992). The average y^+ values for buildings and ground for all cases range between 300–400 and 840–1000, respectively, which fall within the limits where the logarithmic law of the wall is valid (Blocken et al., 2007). An overview of the simulated cases is presented in Table 1.

2.5.4. Grid independence study and overall simulation approach assessment

A grid independence study is conducted to assess the quality of the selected mesh and to ensure that the simulated variables do not depend on grid resolution. Three meshes are analysed: (i) a medium resolution mesh, as described in Section 2.5.2; (ii) a coarse mesh with 21 million cells and (iii) a fine mesh with 75.2 million cells. The representative cell lengths h – that is, the average cell width estimated as the cube root of cell volume – for the coarse, medium and fine meshes are $0.0469H$, $0.0338H$ and $0.0269H$, respectively. According to Celik et al. (2008), the relative difference in h between successive mesh levels should exceed 30%, a condition met in the present study. The target variables are the streamwise velocity U and TKE, which are normalised as U/U_{ref} and k/U_{ref}^2, respectively.

Fig. 5 compares the target variables at two representative locations: immediately upwind of the hospital and in the valley upstream of the area of interest. Using the Richardson extrapolation, the values for an infinitely refined mesh ($h = 0$) are estimated from the medium and fine meshes. The results indicate oscillatory convergence and show that further mesh refinement beyond the medium resolution results in only minimal changes in U/U_H and k/U_H^2. The values from the medium mesh are not significantly different from those extrapolated for $h = 0$. The errors between the medium and fine meshes are quantified using the Grid Convergence Index (GCI) (Roache, 1994, 1997). GCI values at both locations were below 1% for velocity and around 4% for TKE (not shown), indicating that the medium mesh provides nearly grid-independent results. Therefore, the medium-resolution mesh is adopted for the remainder of this study.

In the present study, the assessment of model accuracy and reliability is carried out at two distinct levels. At the mesoscale level, the WRF simulation is validated against observations from 11 meteorological stations during the 2012 Bora event (Appendix), providing evidence that the large-scale driving flow is realistically reproduced. At the building scale, a direct validation against in-situ measurements is not possible due to the absence of observational datasets for extreme Bora wind conditions within the

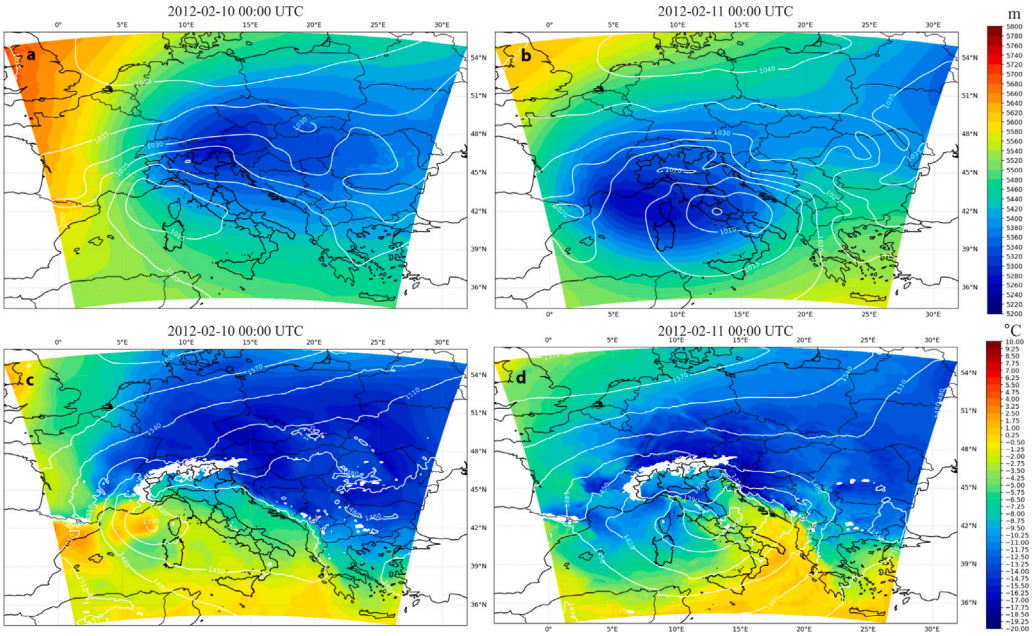

Fig. 6. (a, b) Geopotential heights at 500 hPa (m, colour shading) and mean sea level pressure (*mslp*, hPa, contours) at 00:00 on (a) 10 and (b) 11 February 2012; (c, d) Temperature (°C, colour shading) and geopotential heights (m, contours) at 850 hPa at 00:00 on (c) 10 and (d) 11 February 2012. Data from WRF outermost domain *d*01 (Fig. 2).

Trieste urban area. The reliability of the CFD framework is supported by several complementary factors: the numerical solver has been validated against wind tunnel experiments for both single-building and multi-building configurations in our previous work (Ampatzidis et al., 2022, 2024), while RANS-based approaches have been widely applied to reproduce the basic dynamical processes that characterise a downslope wind like the Bora (e.g. hydraulic jumps, intense shear layers, and terrain-induced recirculation zones). In addition, the computational domain and boundary conditions are constructed following established best-practice guidelines, while the computational mesh has been subjected to a grid independence analysis. These factors provide confidence in the physical consistency and robustness of the simulations.

3. Results and discussion

3.1. Synoptic and mesoscale analysis

Between 10–11 February 2012, an upper-level cut-off low moved westward from eastern Europe towards the central Mediterranean (Fig. 6a, b), accompanied by a cold air mass characterised by widespread temperatures lower than −15 °C at 850 hPa (Fig. 6c, d). The Alpine and Dinaric ridges partially blocked the westward movement of the air mass at the low levels. This peculiar baroclinic situation caused the development of an extratropical cyclone over central Italy (Fig. 6b, Buzzi and Tibaldi 1978). The surface cyclone moved eastward, causing an abrupt intensification of the pressure gradient over the eastern Adriatic coasts (1005 hPa over central Italy; 1030 hPa over eastern Slovenia), triggering violent Bora winds in the Adriatic region (Fig. 6b).

The peak intensity of the Bora winds was reached during the night between 10 and 11 February. In Fig. 7, the wind field at 00:00 on 11 February at different heights is shown, as reproduced by the domain *d*03. At 10 m *AGL* the model simulates the strongest north-easterly winds over the Adriatic Sea (Fig. 7a), with a pattern of alternate banners of stronger and weaker winds, which is a known consequence of the topography of the Dinaric Alps (Grisogono and Belušić, 2009). The relatively weak winds over the land downwind to the Dinaric Alps crests are related to the much stronger roughness and drag of the inland terrain with respect to the maritime surface.

At 950 hPa, the wind field has some notable differences compared to the wind at 10 m *AGL* (Fig. 7b). The winds are more intense over Trieste and the Krk Island, Croatia, with peaks of about 50 m/s. In addition, the wind peaks are shifted from the sea surface to the coastal area. Wind channel can be recognised also at this elevation, while a more uniform east flow is present east of the mountain ridge (the white colour in Fig. 7b, c denotes terrain higher than the pressure level of 950 hPa).

At 850 hPa, the wind speed is weaker and more uniform than at 950 hPa (Fig. 7c). In this case, the wind peaks are located over the mountain crests, and the channels generated by the topography are no longer evident, as the Dinaric Alps have an elevation lower than 1400 m (Fig. 2a), roughly corresponding to the 850 hPa level (Fig. 6d). Finally, at 700 hPa, the Bora winds are not present any more (Fig. 7d). An easterly flow is blowing eastward of the Dinaric Alps, while a convergence zone between southerly winds and weak easterly winds is present over the Istrian peninsula.

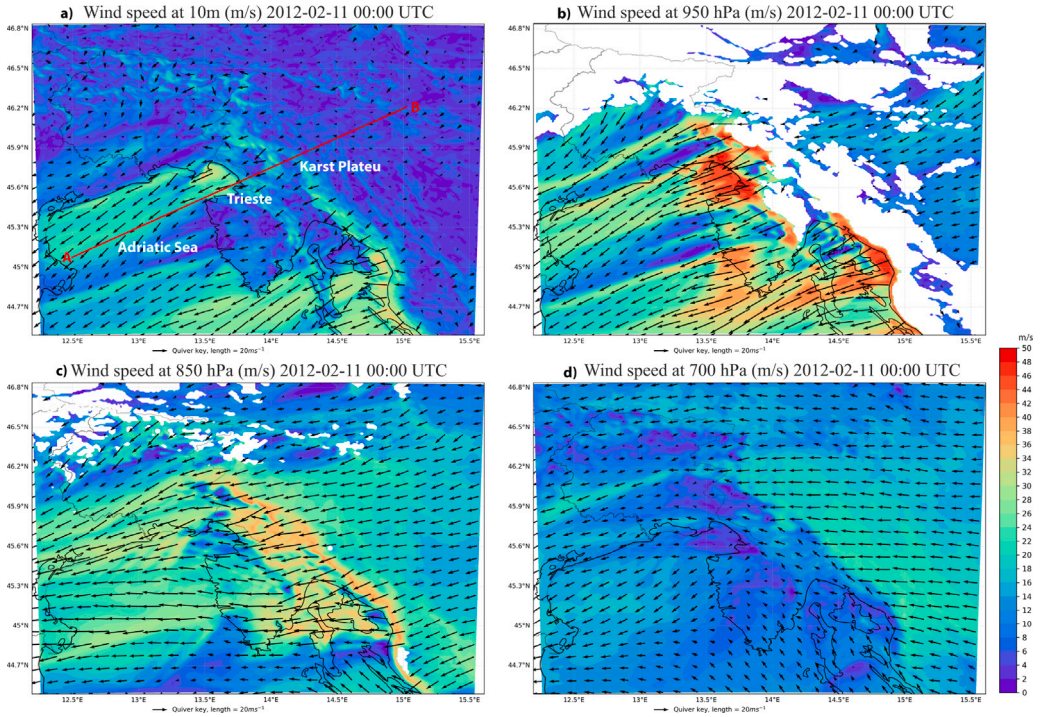

Fig. 7. Wind speed and direction at (a) 10 m *AGL*, (b) 950 hPa, (c) 850 hPa and (d) 700 hPa at 00:00 on 11 February 2012. The plotted domain is *d*03 (see Fig. 2). The line AB in (a) highlights the location of the cross section shown in Fig. 8.

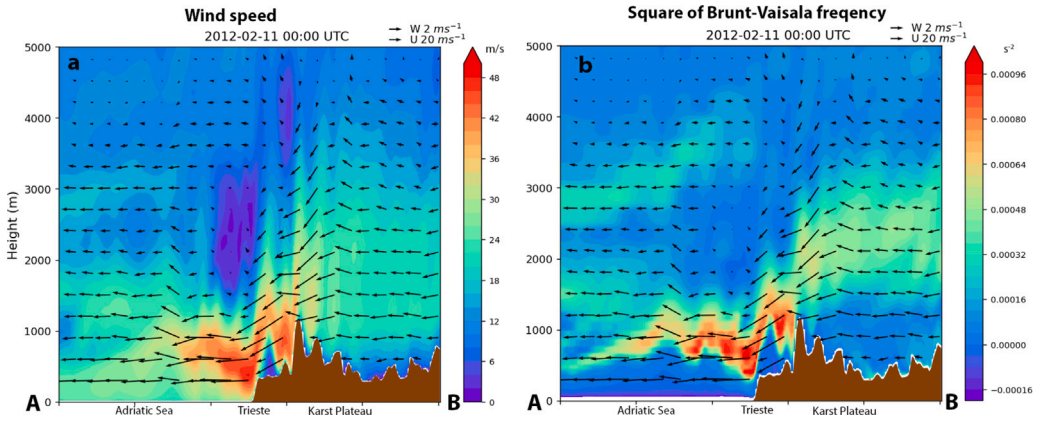

Fig. 8. Cross section AB shown in Fig. 7a: (a) wind speed, (b) square of Brunt–Vaisala frequency at 00:00 on 11 Feb 2012.

To better understand the generation of the Bora winds, a vertical cross section is assessed in Fig. 8. The wind tangential to the cross section is quite uniform between the surface and 3 km *AGL* eastward of the highest Karst peaks (B corner in Fig. 8a), with wind speeds lower than 25 m/s. The Karst peaks generate orographic waves that rapidly break downstream, approximately above the city of Trieste—note the area with zero to very weak wind between 2–3 km *AGL* over Trieste in Fig. 8a. Thus, as the wind passes over the Karst Plateau from $\sim$ 1.5 km above mean sea level (*amsl*), it shifts towards the surface, becoming thinner and stronger. Above the Adriatic Sea, the layer with intense winds weakens and a hydraulic jump feature occurs. The layer with intense winds is shifted from about 300 m *amsl* over Trieste to about 1.5 km *amsl* on the left side of the cross section.

In Fig. 8b, the Brunt–Vaisala frequency, N^2, is plotted along the same cross section together with the tangential wind. N^2 is defined as:

$$N^2 = \frac{g}{\theta}\frac{\partial \theta}{\partial z}, \tag{7}$$

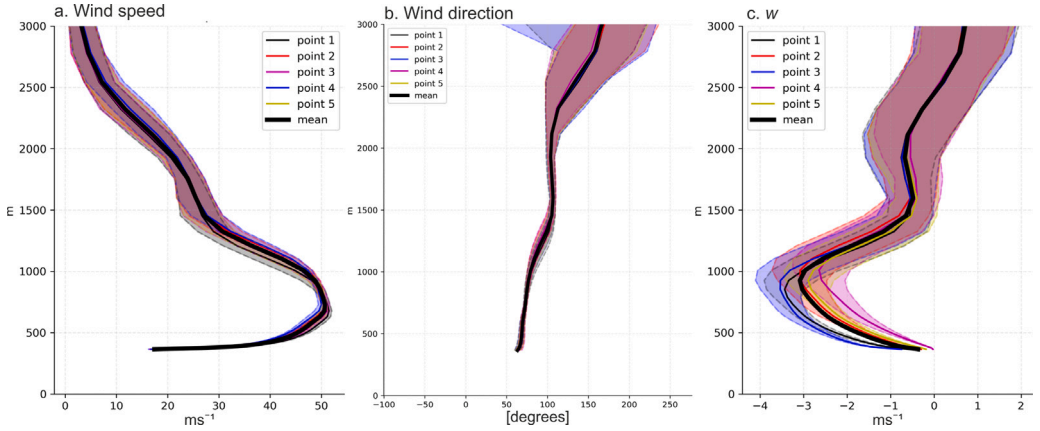

Fig. 9. Vertical profiles of (a) wind speed, (b) wind direction and (d) vertical component of velocity for the five selected grid points (Fig. 3a) used to generate the inflow conditions for the subsequent building-scale simulations. Data sampled for the time window between 03:00 and 05:00 on 11 February 2012. Solid lines are for mean variables, whilst dashed lines denote the 25th and 75th percentiles. The average across the five points is shown with a thicker black solid line. The E on the y axis denotes elevation.

where g is the gravitational acceleration, θ is the potential temperature, and z is the vertical coordinate. The positive values of N^2 in Fig. 8(b) highlight the presence of a stable layer that behaves as an upper limit for the Bora wind. This stable layer is located at 2–3 km *amsl* before impacting the highest Karst peaks; then it intensifies as it descends at an elevation lower than 1 km *amsl*. The stable layer was generated by the continental cold air mass flowing westward (Fig. 6c, d). As shown in previous studies (Durran, 1986; Klemp and Durran, 1987; Markowski and Richardson, 2011), the presence of a stable layer in the low-levels is the crucial feature to generate downslope windstorms. The flow trapped below the stability discontinuity behaves as a hydraulic jump when it crosses a mountain, with streamlines that are compressed close to the surface. This dynamic has also been confirmed for the Bora winds over Trieste by looking at the results of Fig. 8. The pressure gradient between the cyclone over central Italy and the anticyclone over eastern Europe triggers the cold low-level easterly flow. As it interacts with the Dinaric Alps and the Karst plateau, the stable layer generated by the low-level cold air mass causes a hydraulic jump feature downstream of the mountains, responsible for a downslope windstorm along the Adriatic coasts. During the February 2012 event, the Bora winds were particularly strong due to the low-level air mass, which was unusually cold, generating a particularly strong stable layer.

3.2. Derivation of mesoscale-informed inflow conditions

Based on the mesoscale Bora characteristics identified in Section 3.1, representative inflow profiles were extracted from the WRF simulations to initialise the building-scale CFD simulations. Fig. 9 shows the generated profiles from the five selected grid points in the $d04$ domain, including wind speed, wind direction and the vertical component of velocity. A low-level jet profile can be observed with maximum wind speed values of 50 m/s at 730 m *amsl*, and near-zero values at 3 km *amsl* (Fig. 9a). The direction of the wind changes slightly southward from 65° on the surface to 100° at 2 km *amsl* (Fig. 9b). The jet is associated with a downward motion, i.e. negative vertical velocity, that peaks at 930 m *amsl*. The intensity of the downward motion changes slightly among the five points, varying between −2.5 and −3.5 m/s. The downward displacement causes the maximum of the wind speed to appear at an even lower elevation, about 200 m lower (Durran, 1986). In general, the profiles behave similarly, with small variances in the time period considered. Thus, their average is a good proxy for a realistic wind profile to initialise the building-scale simulations.

Fig. 10 presents the turbulent features of the extracted profiles. Close to the ground there is a remarkable mechanical production of turbulence because of the interaction of the surface with the intense low-level jet (Fig. 10a, b). Consequently, TKE is very high near the surface with maximum values larger than 20 m^2/s^2 (Fig. 9c). These values are close to those measured recently by Golem and Večenaj (2023) in Senj, Croatia. At the height which corresponds to the low-level jet, near-zero TKE values are observed. A local secondary maximum appears at $\sim$ 1.5 km *amsl* due to the strong vertical gradient of the wind speed just above the jet level. Finally, the dissipation of TKE, ϵ, logically appears higher close to the ground, whereas a secondary maximum is observed at about 2 km *amsl* due to the large variance generated by small values of the characteristic length, l, calculated by WRF (Fig. 9d).

The final profiles used as inflow conditions for the subsequent building-scale simulations are shown in Fig. 11. All variables and for all cases are normalised using as a reference velocity, U_{ref}, the velocity at 10 m AGL. For the normalisation of ϵ, a reference length, L_{ref}, is also used, as the height of the computational domain at the inlet. The impact of considering the mesoscale information for the generation of the inflow conditions is immediately evident: higher wind speeds across the entire domain height, a more realistic TKE profile – although one should be cautious to interpret the WRF-produced TKE values close to the ground as reality – but similar profiles for the TKE dissipation rate. The W component of the velocity is considered in the inflow conditions of the $WRF-UW$ case only (Table 1).

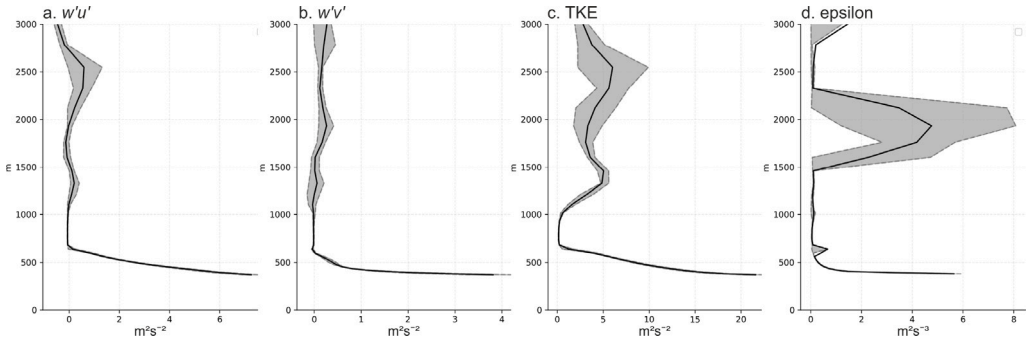

Fig. 10. Vertical profiles of (a) streamwise turbulent fluxes ($\overline{u'u'}$), (b) vertical turbulent fluxes ($\overline{w'v'}$), (c) turbulent kinetic energy (TKE) and (d) dissipation rate of TKE (ϵ) for the five selected grid points (Fig. 3a) used to generate the inflow conditions for the subsequent building-scale simulations. Data sampled for the time window between 03:00 and 05:00 on 11 February 2012. Solid lines for the average profiles across the five points; dashed lines for the 25th and 75th percentiles.

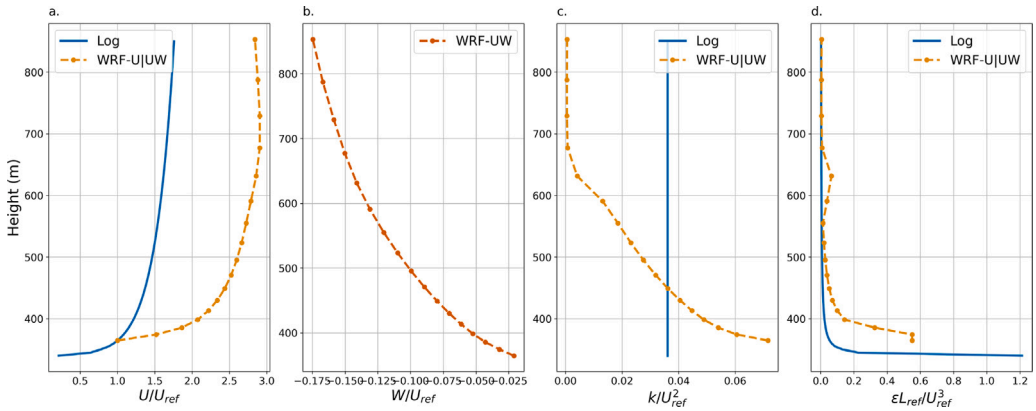

Fig. 11. Inflow vertical profiles of the conducted building-scale simulations. Comparison between the theoretical (Log) and WRF-informed profiles (WRF-U|UW) for (a) streamwise velocity (U/U_{ref}), (b) vertical velocity (W/U_{ref}), (c) turbulent kinetic energy (k/U_{ref}^2), and (d) dissipation rate of TKE ($\varepsilon L_{ref}/U_{ref}^3$). Note that the W component of velocity is considered in the inflow conditions for the $WRF-UW$ case (see Table 1).

3.3. Building-scale simulation results

To facilitate analysis, a structured sampling framework is established as shown in Fig. 12. Four key monitoring points (p1–p4) are selected for the comparison between the CFD and the WRF output in vertical lines to capture spatial variability in atmospheric flow (Fig. 12a). It is worth clarifying that the WRF results should not be considered a benchmark against which to evaluate the results of the CFD simulations; rather, they are presented to compare different model outputs, i.e. a mesoscale model with significant turbulence parametrisation and a small-scale model with direct resolution of the dynamic processes. The four points are placed in symmetrical positions in the open field in order to avoid disturbances from buildings, as the WRF simulations do not take into account explicitly modelled roughness elements. On the windward hospital facade, vertical sampling lines were placed in critical locations to evaluate the distribution of the pressure coefficient (Fig. 12b). Horizontal slices (HS1–HS3) are extracted at 20%, 50%, and 80% of the height of the building to assess the flow field around the two hospital towers (Fig. 12c). Cross-sectional planes (VSX1, VSX2, VSY) are defined to examine the flow structures in the stream and span directions (Fig. 12d).

3.3.1. Assessment of the building-scale simulations

Fig. 13 compares the vertical profiles of normalised streamwise velocity (U/U_{ref}) and TKE (k/U_{ref}^2) at four locations (p1–p4), illustrating the comparison of the building-scale simulation inflow conditions against the mesoscale WRF results. The *Log* case does not reproduce the wind and turbulence structure observed in the WRF profiles. The WRF-informed cases yield velocity profiles that more closely follow the WRF simulation, with $WRF-UW$ generally providing the best agreement. However, while the velocity comparison is meaningful, the interpretation of TKE requires caution. WRF provides partially modelled and partially resolved TKE, with grid spacing that is too coarse near the ground to capture the small-scale turbulence generated by the terrain and flow separation processes. As such, the WRF-generated TKE profiles should not be regarded as the true reference but rather as the most representative estimate of the incoming mesoscale turbulence field available for the analysed Bora event that is used to characterise the CFD

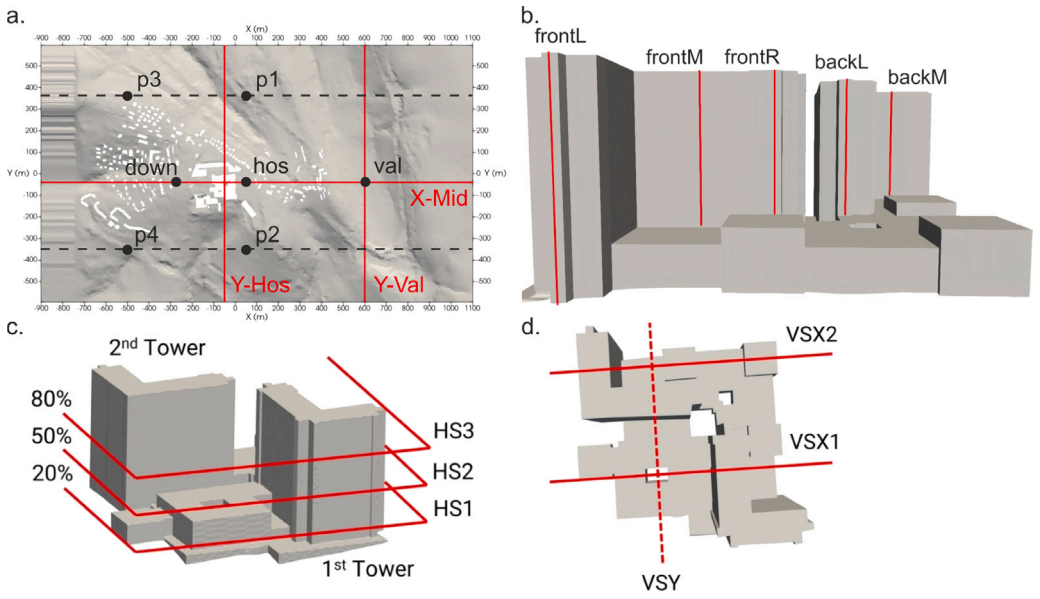

Fig. 12. Overview of the CFD sampling strategy: (a) monitoring points for comparing vertical profiles with the WRF output, streamwise and spanwise sampling lines; (b) vertical facade sampling lines; (c) horizontal slices at 20%, 50%, and 80% of the hospital height; (d) cross-sectional planes.

inflow conditions. This explains why all building-scale cases substantially deviate from the WRF-derived TKE distribution. Overall, the analysis highlights the benefit of using WRF-informed inflows to reproduce the mean velocity structure over complex terrain, while emphasising the limitations of mesoscale modelling in accurately capturing turbulence statistics. Regarding the latter, we acknowledge the greater ability of the CFD models to reproduce the anisotropic nature of near-surface turbulence.

3.3.2. Overall dynamics

Fig. 14 shows contours of velocity magnitude and TKE for the simulated cases in the vertical sampling section $X-Mid$. The Log case shows smooth vertical velocity gradients with a clear increase in wind speed with height, but limited evidence of strong shear and flow separation, characteristic of Bora events. For the WRF-informed simulations, distinct features emerge. In the $WRF-U$ case (Fig. 14b), a pronounced decrease in velocity is observed near the inlet and close to the ground, inside and slightly downstream of the valley, directly associated with a stronger flow separation and the consequent expansion of the recirculation zones within the valley. This effect is a consequence of the increased vertical shear, and thus larger adverse pressure gradient, imposed by the WRF profile, which promotes the development of large separation areas when the flow interacts with the change in elevation. Localised increases in velocity near the hospital are also present, suggesting that the WRF-informed inflow leads to a larger acceleration of the flow as it descends and impinges upon the built environment. A similar but more subdued pattern can be seen in the $WRF-UW$ case (Fig. 14c), where the inclusion of the vertical velocity component reduces the extent of velocity decreases in the valley, while still preserving the increased accelerations near the hospital.

The TKE field complements this interpretation. In the Log case (Fig. 14d), turbulence is distributed more uniformly throughout the domain and does not exhibit the pronounced shear layers observed in the WRF-informed simulations. However, both $WRF-U$ and $WRF-UW$ (Fig. 14e, f) exhibit a well-defined shear interface at about 400 m, which marks the height of the Bora jet. Below this level, TKE is increased due to enhanced shear production, whereas above it, turbulence is suppressed, reflecting the jet's ability to shield the flow aloft from valley-generated disturbances. This structure is consistent with the classical understanding of Bora winds, where a shallow, high-momentum cold jet descends along the terrain. The emergence of this structure demonstrates how the mesoscale information embedded in the inflow conditions propagates into the building-scale simulations and influences the resulting turbulence field. In the $WRF-UW$ case, an intensified turbulence is observed directly on the hospital building, a feature less observed in the $WRF-U$ case.

Fig. 15 depicts vertical profiles of normalised streamwise velocity and TKE at three selected locations as defined in Fig. 12a: within the valley, directly upwind of the hospital complex, and at a location further downwind. In accordance with the results of Fig. 14, in the three locations the WRF-informed cases exhibit higher velocities, with the Log case underestimating the circulation within the valley predicting near-zero or positive streamwise velocities. The inclusion of the downward motion pushes the jet peak to a lower elevation compared to the $WRF-U$ case, resulting in higher turbulence production for $WRF-UW$ below the jet height, approximately at 325 m, and thus lower TKE values above that threshold.

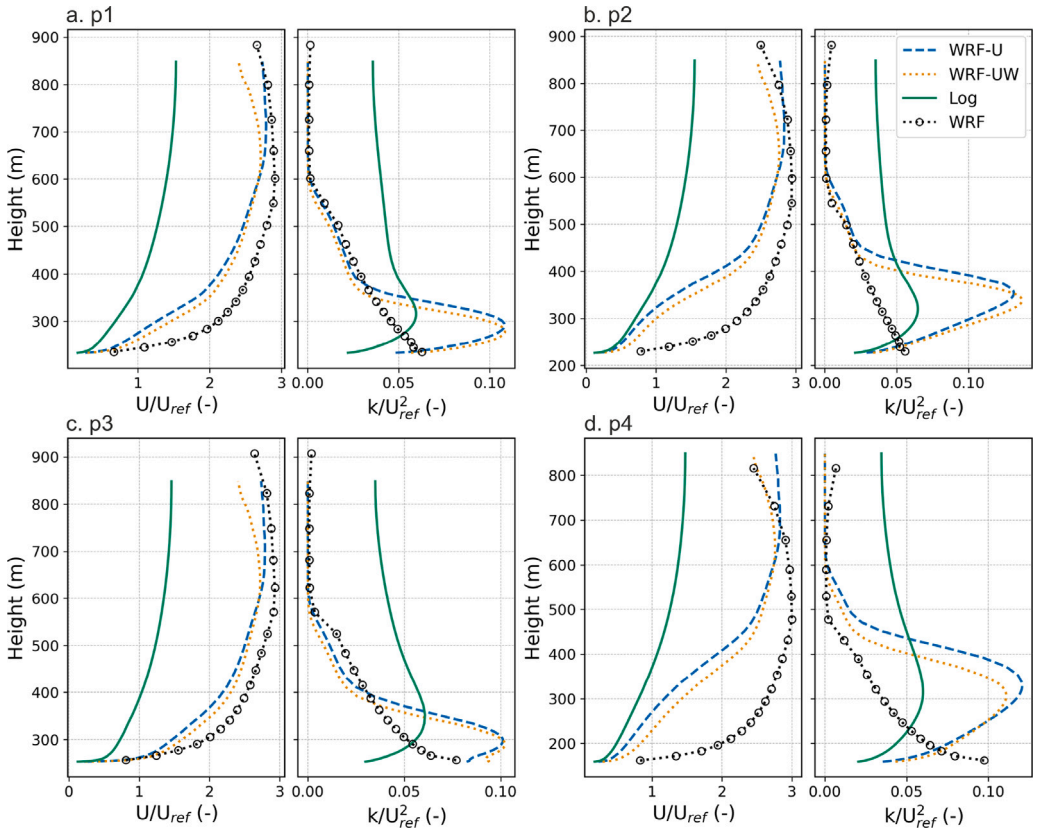

Fig. 13. Comparison between the CFD and WRF vertical profiles of streamwise velocity and TKE at four selected locations within the CFD computational domain (see Fig. 12a for the exact location of the monitoring points p1–p4.

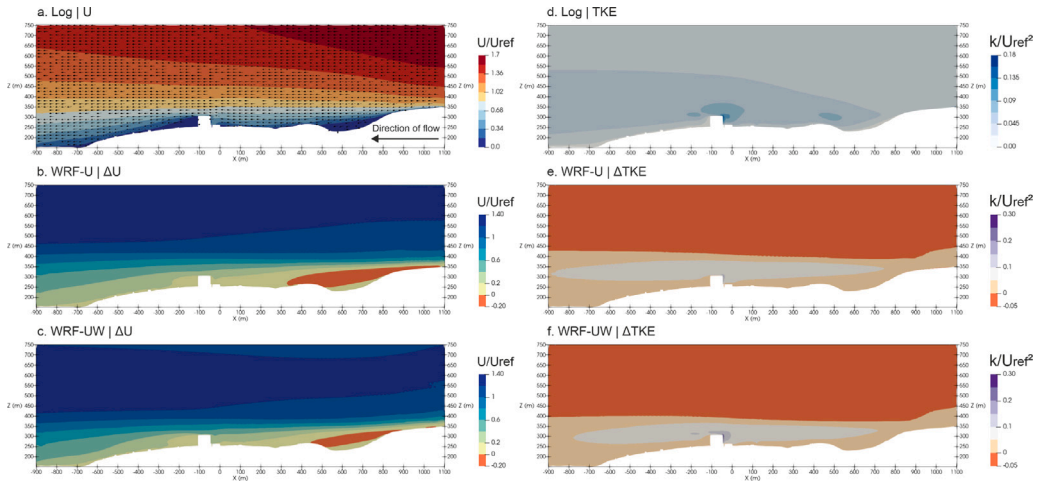

Fig. 14. Velocity magnitude and TKE contours for the simulated cases over the $X - Mid$ sampling section (see Fig. 12. Sub-figures (a) and (d) depict velocity and TKE contours for the *Log* case. Sub-figures (b, c) and (e, f) depict velocity and TKE contours of the difference between the WRF-informed cases against the *Log* case. As the *Log* case shows absolute flow quantities while the WRF-informed ones depict deviations from the *Log* solution, separate colour scales are used to ensure adequate visualisation of the relevant flow structures in each figure.

3.3.3. Wind features around the hospital complex

Fig. 16 depicts velocity and TKE fields over a vertical section in the vicinity of the hospital, revealing marked sensitivities to the choice of inflow conditions. In the *Log* case (Fig. 16a), the velocity field upstream of the hospital displays a gradual vertical shear,

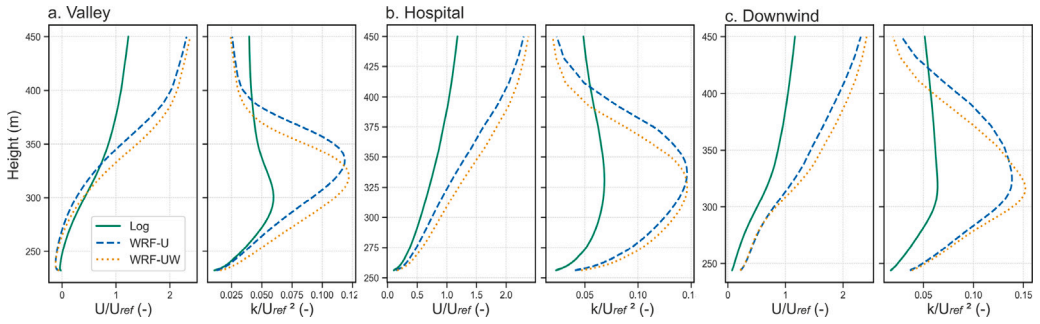

Fig. 15. Vertical profiles of normalised streamwise velocity and TKE for the simulated cases at three locations as defined in Fig. 12a.

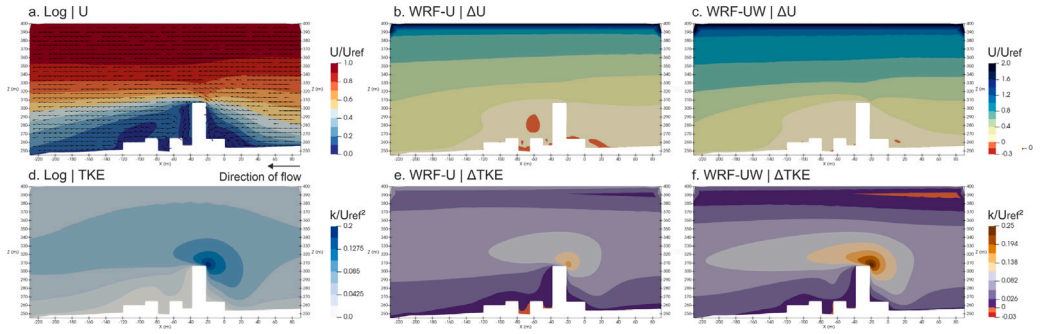

Fig. 16. Velocity magnitude and TKE contours for the simulated cases over the $VSX2$ sampling section (see Fig. 12. Sub-figures (a) and (d) depict velocity and TKE contours for the *Log* case. Sub-figures (b, c) and (e, f) depict velocity and TKE contours of the difference between the WRF-informed cases against the *Log* case. As the *Log* case shows absolute flow quantities while the WRF-informed ones depict deviations from the *Log* solution, separate colour scales are used to ensure adequate visualisation of the relevant flow structures in each figure.

with the highest velocities at and above the roof level. The wake region immediately downstream, and behind the two towers, is characterised by pronounced recirculation areas extending up to approximately 1.5 building heights on the horizontal level, consistent with earlier wind-tunnel investigations of bluff-body aerodynamics in urban environments (Castro and Robins, 1977). In the $WRF-U$ case, reduced velocities are observed in the wake of the building (Fig. 16b). A small region of reduced velocities extends leeward of the hospital, where flow stagnation dominates. Inclusion of the vertical velocity component (Fig. 16c) leads to an increase in velocity in the immediate vicinity of the building, particularly above roof level. This behaviour reflects the interaction between vertical advection and the building-induced flow separation: the downward component of the mesoscale inflow effectively pushes down the shear layer, accelerating the recovery of the mean velocity.

The TKE fields further underscore the role of vertical momentum fluxes. In the *Log* case (Fig. 16d), the high TKE values are mainly confined to the separation area at roof level, with limited penetration aloft. In the WRF-informed cases, TKE experiences increases at roof level, with larger values present in the $WRF-UW$ case. For the latter, the inclusion of the vertical motion leads to a stronger separation and, thus, reduced turbulence production at higher levels. With regard to the WRF-informed cases, this spatial heterogeneity in turbulence production and dissipation highlights the non-linear coupling between mesoscale inflows and building-scale separation dynamics.

Looking at the lowest horizontal section ($HS1$) the near-surface dynamics within and around the hospital complex can be assessed (Fig. 17). In the *Log* case (Fig. 17a), the wind accelerates around windward protrusions and through the inter-building passages, with clear channelisation along the principal gaps. On the downwind side of the buildings, there are extended recirculation areas and corners. The $WRF-U$ case (Fig. 17b) shows widespread positive velocity changes over much of the plan area at this level. Increased velocities are particularly evident across the windward sides of the buildings and in the main inter-building channel; small negative patches are localised in the wake of the building. The $WRF-UW$ case shows weaker velocities and more extensive negative pockets than the $WRF-U$ case, indicating that at the $HS1$ level, $WRF-UW$ produces a larger spatial footprint of reduced velocities.

In terms of TKE, the *Log* case (Fig. 17d) peaks where separation is strongest: at the windward part of the hospital complex, at building corners and side edges, and within the channel where Venturi-type acceleration creates strong lateral shear. In the wake of the buildings, moderate TKE intensities are observed. Both WRF-informed cases lead to generally higher TKE values, albeit with some distinct differences between the two cases: the ΔTKE response for $WRF-U$ is markedly larger in amplitude than for $WRF-UW$, with pronounced positive anomalies wrapped around windward corners, along passages, and at reattachment areas downstream of the main buildings.

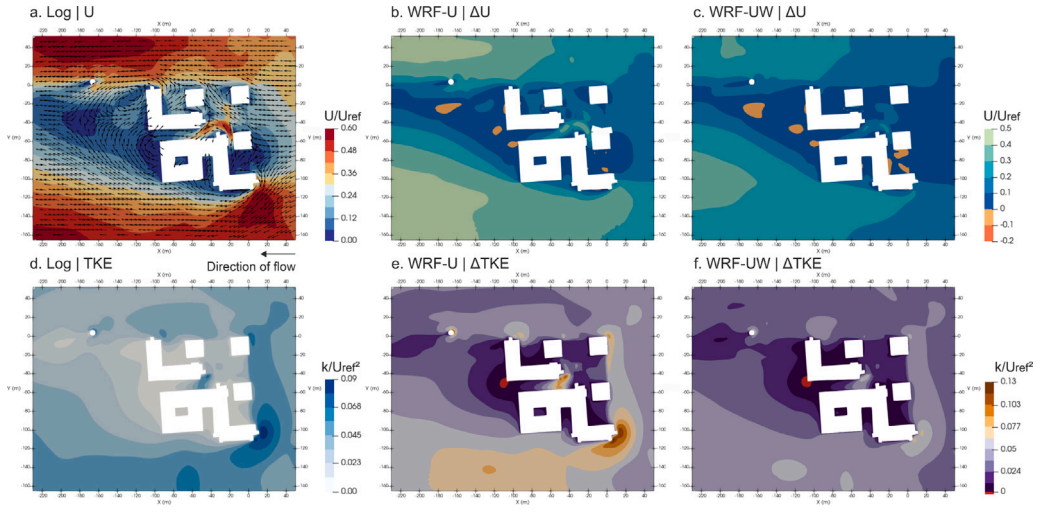

Fig. 17. Velocity magnitude and TKE contours for the simulated cases over the $HS1$ horizontal sampling section (see Fig. 12. Sub-figures (a) and (d) depict velocity and TKE contours for the *Log* case. Sub-figures (b, c) and (e, f) depict velocity and TKE contours of the difference between the WRF-informed cases against the *Log* case. As the *Log* case shows absolute flow quantities while the WRF-informed ones depict deviations from the *Log* solution, separate colour scales are used to ensure adequate visualisation of the relevant flow structures in each figure.

In regard to the higher horizontal slice $HS2$, the *Log* case (Fig. 18a) shows the typical features of flow acceleration around the windward corners and along the narrow passage, strong lateral gradients from where flow squeezes between the two main buildings, and recirculation regions in the lee of the buildings. Unlike the $HS1$ level, the $WRF-U$ case shows larger areas of negative ΔU and weaker velocity increases than $WRF-UW$, especially within the narrow passage, the lee building edges, and the main wake areas, and in broad regions downstream of the hospital complex. Regarding TKE, the *Log* case exhibits more intense turbulence in the windward areas, especially around the sharp corners of the buildings and within the narrow passage. The WRF-informed cases present a systematically larger turbulence intensity across the board, but the inclusion of the vertical component of velocity increases the vertical transfer of momentum from the mesoscale field and, thus, the impinging flow has more downward momentum transport that produces larger TKE changes. Indeed, the $WRF-UW$ case experiences a larger and more spatially extensive positive ΔTKE than the $WRF-U$ case. Results at the $HS3$ plane are similar to $HS2$ and, thus, not shown here for brevity.

Overall, the results suggest that the $WRF-UW$ case leads to concentration of mean momentum and shear production at higher elevations ($HS2$) while the immediate layer below ($HS1$) experiences a relative deceleration or less turbulence production because the downward momentum is partly consumed near the roof level. In other words, $WRF-UW$ injects momentum downwards but that momentum is converted into horizontal kinetic energy and turbulent production at higher levels ($HS2$ and $HS3$—results for the latter are omitted for simplicity); at $HS1$ the result can be broader low-speed areas and reduced TKE compared to the case where the W component is ignored.

3.3.4. Wind load on buildings

The surface pressure acting on the building is described by pressure coefficients, calculated by normalisation with the velocity pressure in the undisturbed approaching wind at the height of the building. For an incompressible flow, the equation reads $Cp = (P_k - P_{k0})/0.5U_H^2$, where P_k is the kinematic pressure on the building facade, P_{k0} is the reference kinematic pressure and U_H is the reference velocity at the hospital height. Fig. 19 shows the Cp profiles in five locations along the windward facade of the building complex. The profiles exhibit a typical distribution of Cp in tall buildings with values increasing with height (Abu-Zidan et al., 2020). The choice of inflow conditions has a profound influence on facade pressurisation. The *Log* case systematically underpredicts Cp, reaching values of only ~0.5–0.8 at roof height. In contrast, both WRF-informed cases yield substantially higher pressure coefficients, with values between ~1.0 and 2.3, with the discrepancies compared to the *Log* case increasing with height. Interestingly, systematic differences emerge between $WRF-U$ and $WRF-UW$. In all locations, $WRF-U$ produces the largest facade pressurisation, exceeding $WRF-UW$ by up to 10% on average. The inclusion of vertical mesoscale velocity in the $WRF-UW$ case reduces Cp, particularly at higher elevations. This behaviour can be explained by the additional downward momentum and enhanced vertical mixing introduced by the negative mesoscale W, which redistributes streamwise momentum vertically, weakens horizontal stagnation, and reduces the pressure on the facade.

The magnitude of these differences is quantified in Fig. 20, which highlights the sensitivity of the predicted facade pressures to the imposed inflow conditions. For the front building, the average Cp of $WRF-U$ is ~430% higher than *Log* and ~0.1% higher than $WRF-UW$, while for the back building the differences increase to ~900% and ~9%, respectively. These findings highlight the importance of mesoscale–microscale coupling: while WRF-informed simulations increase facade loads, the specific treatment of vertical momentum fluxes controls the partitioning between horizontal pressurisation and vertical redistribution of kinetic energy.

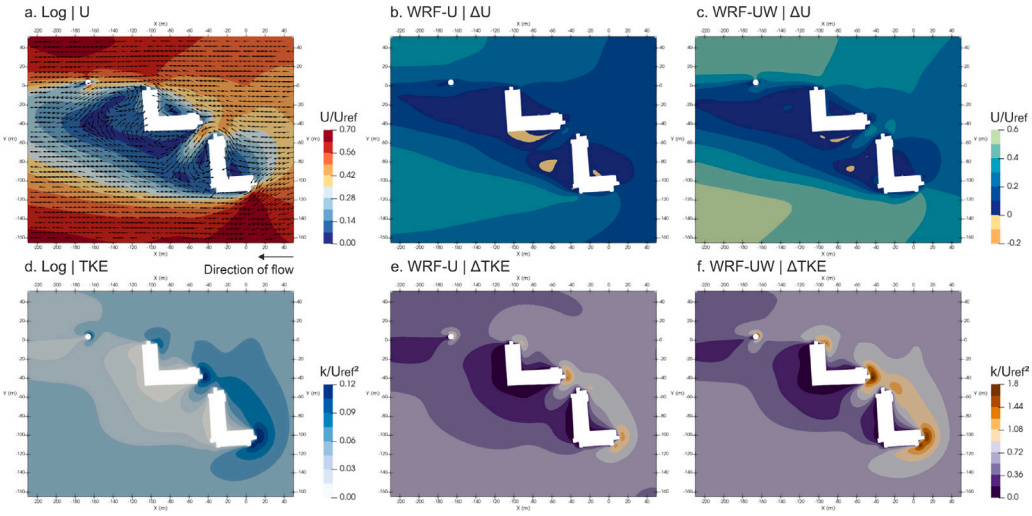

Fig. 18. Velocity magnitude and TKE contours for the simulated cases over the $HS2$ horizontal sampling section (see Fig. 12). Sub-figures (a) and (d) depict velocity and TKE contours for the *Log* case. Sub-figures (b, c) and (e, f) depict velocity and TKE contours of the difference between the WRF-informed cases against the *Log* case. As the *Log* case shows absolute flow quantities while the WRF-informed ones depict deviations from the *Log* solution, separate colour scales are used to ensure adequate visualisation of the relevant flow structures in each figure.

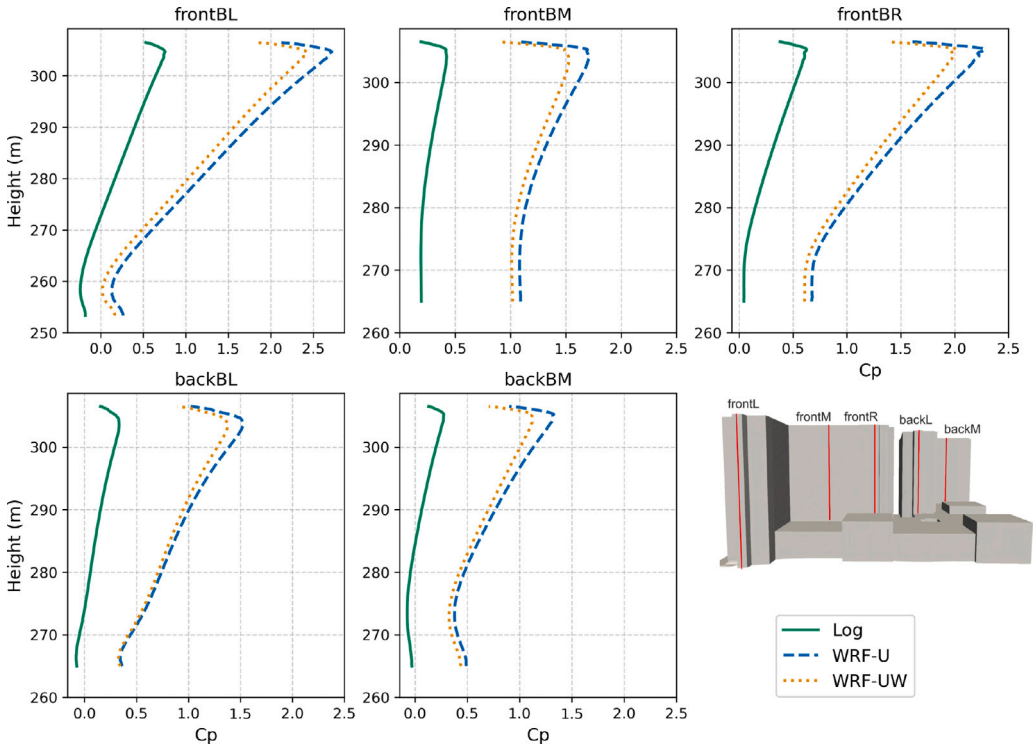

Fig. 19. Pressure coefficient (Cp) profiles on five selected locations along the windward facades of the hospital complex.

3.4. Future perspectives

The adopted downscaling methodology, which employs steady-state RANS simulations, provides an effective approach to reproduce the mean flow characteristics of the peak quasi-stationary phase of the extreme Bora event studied here. RANS simulations resolve only the time-averaged flow field and therefore do not capture transient phenomena such as unsteady turbulent motions and the temporal evolution of gust structures. This limitation of RANS is consistent with the scope of this work that focuses on how

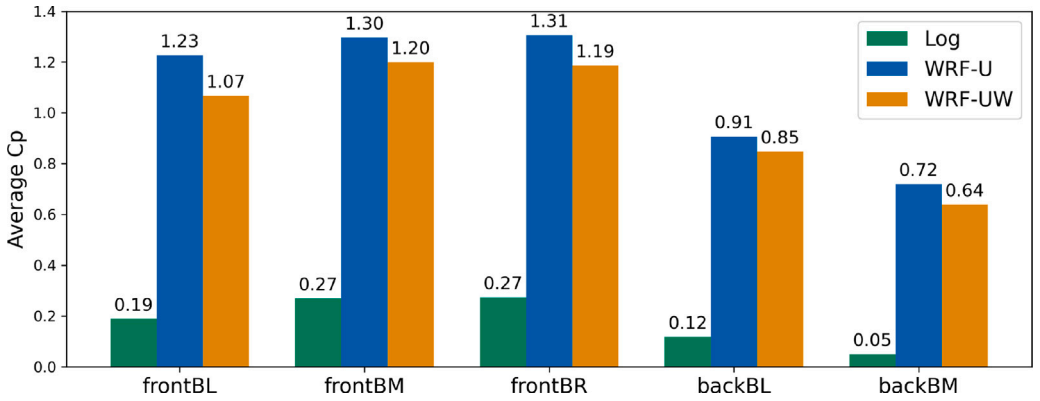

Fig. 20. Average pressure coefficients (Cp) for the five selected locations along the windward facades of the hospital complex.

different inflow formulations influence the mean building-scale flow field, turbulence distribution, and atmospheric loading during an extreme Bora event.

Resolving the transient turbulent structures and instantaneous gust-induced loads would require higher-fidelity unsteady approaches such as LES. However, such extensions are not straightforward, as higher-fidelity simulations require physically consistent time-dependent turbulent inflow conditions rather than mean atmospheric profiles as those employed here. While WRF-derived mean flow quantities can be transferred naturally into a RANS framework, the generation of realistic turbulent inflow fields for LES remains an active area of meso-microscale coupling research. The development and validation of such approaches for extreme windstorms present a promising direction for future work.

Lastly, the need for field campaigns during extreme wind events has become increasingly important. Observational efforts for the characterisation of the atmospheric boundary layer during such events will provide further insight into the real-world impact of windstorms on urban infrastructure and support the continued refinement of multiscale methodologies for the analysis of extreme winds.

4. Conclusions

In this study, a multiscale numerical methodology is introduced and evaluated to investigate the impact of an extreme wind event on a hospital building over complex terrain. By explicitly downscaling weather data obtained from the Weather Research and Forecasting (WRF) model and incorporating mesoscale information into building-scale simulations, including both horizontal and vertical wind components, key limitations of conventional practice, where idealised logarithmic inflow profiles are typically prescribed, were overcome. The approach applied here enables a more physically consistent representation of the inflow and its interaction with the complex topography.

The downscaling of weather variables significantly altered the near-surface flow structure. In the valley upstream of the hospital, WRF-informed simulations captured enhanced wind recirculation areas, while also exhibiting a well-defined shear interface, marking the height of the Bora low-level jet. The logarithmic case could not reproduce these dynamics. The simulations that included the vertical velocity component showed larger positive changes in velocity and TKE closer to the ground, demonstrating that mesoscale flow information can exert a non-negligible control on the microscale dynamics.

The results demonstrated that mesoscale inflows do not simply increase or decrease turbulence uniformly across the domain height but redistribute energy across layers. Analysis at the hospital site revealed that the inclusion of the vertical velocity component generally produces higher TKE values below 325 m, while the reverse is true above this level. Regarding pressure coefficients, the logarithmic case systematically underestimates windward pressures on the building. Interestingly, we found that the inclusion of the mesoscale vertical velocity leads to decreased pressure coefficients – compared to the mesoscale-informed case that includes only the streamwise velocity – as it reduces the peak stagnation pressures by redistributing horizontal momentum vertically and enhancing mixing.

To the best of our knowledge, this is the first study to explicitly demonstrate, for an extreme windstorm, how mesoscale-informed inflow conditions and terrain-induced downdrafts modify microscale wind and turbulence fields, and how these changes affect the atmospheric load on buildings. The results illustrate the limitations of traditionally used logarithmic inflow profiles in contexts where extreme events and complex terrain dominate flow dynamics.

This type of analysis gains particular relevance in the context of climate change, as growing evidence suggests that the frequency and intensity of extreme wind events will increase. Buildings and critical infrastructures must be prepared to withstand the impacts of extreme winds, an environmental hazard that has largely been overlooked to date in comparison with other climate-related risks. For critical infrastructures such as hospitals, the primary risk is not necessarily structural failure, but rather the loss of functionality caused by wind-induced damage to façades, rooftops, technical installations, and access routes. Such disruptions can severely compromise emergency response and healthcare delivery. By enabling a more realistic reproduction of wind loads, turbulence levels, and flow structures under extreme conditions, numerical approaches such as the one presented here strengthen the physical basis upon which risk and resilience assessments are performed.

Table A.1
Configuration of the WRF simulations, including details on the adopted sub-models and numerical schemes.

Name	PBL scheme	Microphysics scheme	First vertical level	Radiation scheme	Land surface model
Yon_Tom	Yonsei University	Thompson	5 m AGL	RRTMG	Noah-MP
MYJ_Tom	Mellor–Yamada–Janjic	Thompson	5 m AGL	RRTMG	Noah-MP
MYJ_Tom_vl	Mellor–Yamada–Janjic	Thompson	10 m AGL	RRTMG	Noah-MP
acm2_px	ACM2	Thompson	5 m AGL	RRTMG	Pleim-Xiu
MYJ_Dou6cl	Mellor–Yamada–Janjic	WRF Double-momentum 6-class	5 m AGL	RRTMG	Noah-MP
MYJ_Tom_rad	Mellor–Yamada–Janjic	Thompson	5 m AGL	RRTM-Dudhia	Noah
Yon_Tom_noah	Yonsei University	Thompson	5 m AGL	RRTMG	Noah
BouLac_Tom	Boulac	Thompson	5 m AGL	RRTMG	Noah-MP
Yon_Tom_rad	Yonsei University	Thompson	5 m AGL	RRTM-Dudhia	Noah

CRediT authorship contribution statement

Petros Ampatzidis: Writing – review & editing, Writing – original draft, Visualization, Software, Methodology, Investigation, Formal analysis, Conceptualization. **Carlo Cintolesi:** Writing – review & editing, Supervision, Software, Resources, Methodology, Conceptualization. **Francesco De Martin:** Writing – review & editing, Visualization, Validation, Software, Formal analysis. **Andrea Petronio:** Writing – review & editing, Software, Methodology. **Andrea Zonato:** Writing – review & editing, Software. **Silvana Di Sabatino:** Writing – review & editing, Supervision, Project administration, Funding acquisition, Conceptualization.

Declaration of competing interest

The authors declare that they have no known competing financial interests or personal relationships that could have appeared to influence the work reported in this paper.

Acknowledgements

This work was supported by the RISKADAPT project, funded by the European Union HORIZON research and innovation programme under grant agreement No. 101093939. The authors acknowledge the use of computational resources from the parallel computing cluster of the Open Physics Hub at the Department of Physics and Astronomy ‘Augusto Righi’ at the University of Bologna, Italy.

Appendix. Validation of the WRF simulations

A sensitivity study is conducted to assess the accuracy of different sets of physical parametrisation suites, as shown in Table A.1. The choice of the tested physical parametrisations was inspired by previous numerical experiments conducted for similar events (Park et al., 2022; Cao and Fovell, 2016).

Downslope windstorms are strongly influenced by surface exchanges between the ground and the atmosphere (Cao and Fovell, 2018), thus four experiments are performed to assess the sensitivity to the PBL scheme: the Yonsei University scheme (Hong et al., 2006), the Mellor–Yamada–Yanjic (MYJ, Mellor and Yamada, 1982; Janjić, 1994), the Asymmetric Convective Model scheme (ACM2, Pleim, 2007) - which requests the Pleim-Xiu land surface model (Pleim, 2006), and the BouLac scheme (Bougeault and Lacarrere, 1989) are tested. For microphysics processes, two schemes are assessed, namely the Thompson scheme (Thompson et al., 2008) and the WRF Double-momentum 6-class scheme (Hong and Lim, 2006). The test on microphysics was conducted because during the Bora event there was some precipitation on the upwind side of the Karst plateau. Two land surface models are used: the Noah-MP (Niu et al., 2011) with the revised MM5 scheme (Jiménez et al., 2012) for surface physics, and the simple Noah land surface model (Mukul Tewari et al., 2004). Two radiation scheme configurations are implemented: one using the rapid radiative transfer model for global climate models (RRTMG) scheme for long-wave and short-wave radiation (Iacono et al., 2008), and the other using the RRTM (Mlawer et al., 1997) for long-wave radiation, and the Dudhia scheme (Dudhia, 1989) for short-wave radiation.

The results of the innermost domain $d04$ are compared with data from 11 ground weather stations obtained from ARPA FVG (Fig. 2b). The validation is performed on the Italian side of the domain, i.e. the downwind side of the Bora wind. At the weather stations, hourly values of 2 m temperature, 2 m relative humidity, 10 m maximum wind gusts, 10 m instantaneous wind speed, and 10 m wind direction are considered. The values are averaged across the 11 locations, whilst the targeted time period is the two full days, 10 and 11 February 2012. Three statistical metrics are computed for the averaged values, namely Pearson correlation coefficient (r), bias error and Root Mean Square Error (RMSE).

Table A.2 presents validation results for the 2 m air temperature and relative humidity. Results show that the simulations accurately reproduce both variables with small discrepancies from the observed values. More specifically, simulations tend to slightly underestimate air temperatures with RMSE values around 1 °C, with low biases of less than 1 °C and high correlation factors of more than 0.6 on average. Regarding relative humidity, RMSE values are lower than 15%, biases are about 10% on average, and correlations are about 0.5. Overall, the *Yon_Tom_rad* simulation demonstrates the best agreement.

Table A.2
WRF validation results against observational data for air temperature and relative humidity. Statistical metrics include Pearson correlation coefficient (r), bias and RMSE.

Model name	2 m temperature			2 m relative humidity		
	r	Bias (°C)	RMSE (°C)	r	Bias (%)	RMSE (%)
Yon_Tom	0.63	−0.9	1.2	0.51	7.7	9.6
MYJ_Tom	0.57	**−0.6**	1.2	0.47	12.0	13.3
MYJ_Tom_vl	0.60	−1.0	1.4	0.45	13.3	14.4
acm2_px	0.55	**−0.5**	**1.0**	**0.56**	9.4	10.9
MYJ_Dou6cl	0.60	−0.8	1.3	0.48	9.9	11.6
MYJ_Tom_rad	**0.75**	**−0.6**	1.1	0.46	11.6	13.1
Yon_Tom_noah	0.58	−1.1	1.4	0.43	11.7	12.7
BouLac_Tom	0.66	0.8	1.1	0.45	**4.1**	**9.1**
Yon_Tom_rad	**0.69**	−0.7	**1.0**	**0.52**	**7.0**	**9.2**

Table A.3
Validation results of the WRF model against observational data for wind gusts (WG) and wind speed (WS) at 10 m AGL. Statistical metrics include Pearson correlation coefficient (r), bias and RMSE.

Model name	Wind gusts			Wind speed		
	r	Bias (m/s)	RMSE (m/s)	r	Bias (m/s)	RMSE (m/s)
Yon_Tom	0.56	−6.9	8.2	0.48	**0.5**	**3.5**
MYJ_Tom	0.61	**−5.9**	7.6	0.49	1.6	3.9
MYJ_Tom_vl	0.60	−6.4	7.8	0.49	1.6	4.1
acm2_px	**0.64**	−7.3	8.2	**0.54**	1.6	3.9
MYJ_Dou6cl	0.58	−6.2	7.7	0.44	1.6	4.3
MYJ_Tom_rad	0.60	−6.3	8.0	0.49	1.3	4.0
Yon_Tom_noah	0.61	**−3.9**	**6.3**	0.47	3.0	4.8
BouLac_Tom	**0.71**	−6.8	**7.6**	**0.55**	2.7	4.1
Yon_Tom_rad	0.58	−6.6	7.9	0.48	**0.6**	**3.6**

Table A.4
Validation results of the WRF model against observational data for wind direction (WD) at 10 m AGL. Statistical metrics include Pearson correlation coefficient (r), bias and RMSE.

	Wind direction		
Model name	r	Bias (°)	RMSE (°)
Yon_Tom	0.10	8.4	38.1
MYJ_Tom	**0.20**	5.5	27.6
MYJ_Tom_vl	**0.20**	**3.1**	24.8
acm2_px	0.09	4.7	26.9
MYJ_Dou6cl	**0.20**	**1.2**	**24.1**
MYJ_Tom_rad	0.13	4.9	30.2
Yon_Tom_noah	0.15	7.3	34.4
BouLac_Tom	**0.27**	3.7	**16.4**
Yon_Tom_rad	0.11	10.6	41.3

Tables A.3 and A.4 present the validation results for the wind variables at 10 m AGL. Results show that the simulations tend to underestimate wind gusts with an average bias of about 6 m/s. This is in agreement with Cao and Fovell (2018), who observed similar behaviour when studying a downslope windstorm in the United States; WRF was found unable to resolve the very fast and local turbulent characteristics of the wind gusts, causing a systematic underestimation of their magnitude. The model also struggles to accurately predict wind direction with quite large RMSE values and low Pearson correlations. This could be attributed to the fact that in reality the wind direction changes locally due to the presence of small-scale obstacles, such as buildings or trees, that are not considered in the model. However, looking closer to the simulations, the wind reproduction near the Cattinara hospital agrees better with the observations, with RMSE values of about 10 °C. This implies that a weather station above the hill leads to better agreement with the observations because it is more isolated from surface obstacles that can influence the wind direction locally. The instantaneous wind speed demonstrates lower RMSE values (about 4 m/s) and biases (about 1 m/s) than the other two variables, suggesting that the simulations are overall capable of reproducing the strong Bora wind speeds, which were often above 20 m/s near the surface with gusts exceeding 30 m/s.

According to Table A.3, there is no simulation that outperforms the others. Some simulations exhibit better agreement on wind direction (*MYJ_Dou6cl*), others on wind speed (*Yon_Tom_rad*) or on maximum wind gusts (*Yon_Tom_rad*). As the objective of the mesoscale simulations is to provide inlet profiles for the subsequent building-scale simulations, the selected model should be able to provide the parametrised TKE as an output. The only model offering this possibility is *MYJ_Tom_rad*, and thus is selected as the preferred model for this work—it is also the model that performs best compared to the other PBL schemes that employ MYJ.

Data availability

No data was used for the research described in the article.

References

Abu-Zidan, Y., Mendis, P., Gunawardena, T., 2020. Impact of atmospheric boundary layer inhomogeneity in CFD simulations of tall buildings. Heliyon 6 (7).

Alpers, W., Ivanov, A., Horstmann, J., 2009. Observations of bora events over the adriatic sea and black sea by spaceborne synthetic aperture radar. Mon. Weather Rev. 137 (3), 1150–1161.

Ampatzidis, P., Cintolesi, C., Di Sabatino, S., Kershaw, T., 2024. Blue space effects on urban flow and pollution dispersion in a stable atmosphere. Urban Clim. 55, 101898.

Ampatzidis, P., Cintolesi, C., Petronio, A., Di Sabatino, S., Kershaw, T., 2022. Evaporating waterbody effects in a simplified urban neighbourhood: A RANS analysis. J. Wind Eng. Ind. Aerodyn. 227, 105078.

Avolio, E., Miglietta, M.M., Fanelli, C., Lagasio, M., Mengistu, M.T., Milelli, M., Parodi, A., Xhelaj, A., Burlando, M., 2026. Analysis of the 18 August 2022 western Mediterranean derecho: Atmospheric dynamics and impacts over the northwestern Italian coast. Atmos. Res. 336, 108858.

Babić, N., Večenaj, Ž., Kozmar, H., Horvath, K., De Wekker, S.F., Grisogono, B., 2016. On turbulent fluxes during strong winter bora wind events. Bound.-Layer Meteorol. 158 (2), 331–350.

Beg Paklar, G., Isakov, V., Koračin, D., Kourafalou, V., Orlić, M., 2001. A case study of bora-driven flow and density changes on the Adriatic Shelf (January 1987). Cont. Shelf Res. 21 (16), 1751–1783.

Belušić, D., Žagar, M., Grisogono, B., 2007. Numerical simulations of pulsations in the bora wind. Q. J. R. Meteorol. Soc. 133 (627), 1371–1388.

Belušić Vozila, A., Belušić, D., Telišman Prtenjak, M., Güttler, I., Bastin, S., Brisson, E., Demory, M.E., Dobler, A., Feldmann, H., Hodnebrog, Ø., et al., 2024. Evaluation of the near-surface wind field over the Adriatic region: local wind characteristics in the convection-permitting model ensemble. Clim. Dyn. 62 (6), 4617–4634.

Bilal, M., Birkelund, Y., Homola, M., Virk, M.S., 2016. Wind over complex terrain – Microscale modelling with two types of mesoscale winds at Nygårdsfjell. Renew. Energy 99, 647–653.

Blocken, B., 2014. 50 years of Computational Wind Engineering: Past, present and future. J. Wind Eng. Ind. Aerodyn. 129, 69–102.

Blocken, B., 2015. Computational Fluid Dynamics for urban physics: Importance, scales, possibilities, limitations and ten tips and tricks towards accurate and reliable simulations. Build. Environ. 91, 219–245, Fifty Year Anniversary for Building and Environment.

Blocken, B., Stathopoulos, T., Carmeliet, J., 2007. CFD simulation of the atmospheric boundary layer: wall function problems. Atmos. Environ. 41 (2), 238–252.

Boldrin, A., Carniel, S., Giani, M., Marini, M., Bernardi Aubry, F., Campanelli, A., Grilli, F., Russo, A., 2009. Effects of bora wind on physical and biogeochemical properties of stratified waters in the northern Adriatic. J. Geophys. Res.: Ocean. 114 (C8), https://agupubs.onlinelibrary.wiley.com/doi/abs/10.1029/2008JC004837.

Bougeault, P., Lacarrere, P., 1989. Parameterization of orography-induced turbulence in a mesobeta–scale model. Mon. Weather Rev. 117 (8), 1872–1890.

Buzzi, A., Tibaldi, S., 1978. Cyclogenesis in the lee of the Alps: A case study. Q. J. R. Meteorol. Soc. 104 (440), 271–287.

Cao, Y., Fovell, R.G., 2016. Downslope windstorms of San Diego County. Part I: a case study. Mon. Weather Rev. 144 (2), 529–552.

Cao, Y., Fovell, R.G., 2018. Downslope windstorms of San Diego County. Part II: Physics ensemble analyses and gust forecasting. Weather. Forecast. 33 (2), 539–559.

Castorrini, A., Gentile, S., Geraldi, E., Bonfiglioli, A., 2021. Increasing spatial resolution of wind resource prediction using NWP and RANS simulation. J. Wind Eng. Ind. Aerodyn. 210, 104499.

Castorrini, A., Gentile, S., Geraldi, E., Bonfiglioli, A., 2023. Investigations on offshore wind turbine inflow modelling using numerical weather prediction coupled with local-scale computational fluid dynamics. Renew. Sustain. Energy Rev. 171, 113008.

Castro, I.P., Robins, A.G., 1977. The flow around a surface-mounted cube in uniform and turbulent streams. J. Fluid Mech. 79 (2), 304–355.

Celik, I.B., Ghia, U., Roache, P.J., Freitas, C.J., Coleman, H., Raad, P.E., 2008. Procedure for estimation and reporting of uncertainty due to discretization in CFD applications. J. Fluids Eng. 130 (7), 078001.

Cintolesi, C., Grenzi, M., Guidetti, L., Baldini, L., Di Sabatino, S., Porcù, F., 2026. Revealing atmospheric Von Kármán vortex street past a severe thunderstorm. Mon. Weather Rev. e250266.

Dagnew, A., Bitsuamlak, G.T., 2013. Computational evaluation of wind loads on buildings: a review. Wind. Struct 16 (6), 629–660.

Davolio, S., Stocchi, P., Benetazzo, A., Bohm, E., Riminucci, F., Ravaioli, M., Li, X.M., Carniel, S., 2015. Exceptional Bora outbreak in winter 2012: Validation and analysis of high-resolution atmospheric model simulations in the northern Adriatic area. Dyn. Atmos. Oceans 71, 1–20.

De Martin, F., Zonato, A., Di Sabatino, S., 2025. Effects of the urban land use on a severe convective windstorm. Q. J. R. Meteorol. Soc. 151 (773), e5058.

Dorman, C.E., Carniel, S., Cavaleri, L., Sclavo, M., Chiggiato, J., Doyle, J., Haack, T., Pullen, J., Grbec, B., Vilibić, I., Janeković, I., Lee, C., Malačič, V., Orlić, M., Paschini, E., Russo, A., Signell, R.P., 2006. February 2003 marine atmospheric conditions and the bora over the northern Adriatic. J. Geophys. Res.: Ocean. 111 (C3).

Dudhia, J., 1989. Numerical study of convection observed during the winter monsoon experiment using a mesoscale two-dimensional model. J. Atmos. Sci. 46 (20), 3077–3107.

Dudhia, J., 2014. A history of mesoscale model development. Asia-Pacific J. Atmos. Sci. 50 (1), 121–131.

Durán, P., Meißner, C., Casso, P., 2020. A new meso-microscale coupled modelling framework for wind resource assessment: A validation study. Renew. Energy 160, 538–554.

Durran, D.R., 1986. Another look at downslope windstorms. Part I: The development of analogs to supercritical flow in an infinitely deep, continuously stratified fluid. J. Atmos. Sci. 43 (21), 2527–2543.

EC, 2021. Forging a Climate-Resilient Europe - The New EU Strategy on Adaptation to Climate Change. Technical Report, European Commission, SEC(2021) 89 final.

Enger, L., Grisogono, B., 1998. The response of bora-type flow to sea surface temperature. Q. J. R. Meteorol. Soc. 124 (548), 1227–1244.

ESI-OpenCFD, 2020. OpenFOAM®, OpenCFD Ltd Release version 2006. web: https://www.openfoam.com/news/main-news/openfoam-v20-06. (Accessed on 28 March 2024).

Fernando, H., 2010. Fluid dynamics of urban atmospheres in complex terrain. Annu. Rev. Fluid Mech. 42 (1), 365–389.

Franke, J., Hellsten, A., Schlünzen, H., Carissimo, B., 2007. Best practice guideline for the CFD simulation of flows in the urban environment. COST Action 732.

Garuma, G.F., 2018. Review of urban surface parameterizations for numerical climate models. Urban Clim. 24, 830–851.

Golem, P., Večenaj, Ž., 2023. The effect of orography on bora wind turbulence. Bound.-Layer Meteorol. 187 (1), 193–212.

Greenshields, C., Weller, H., 2022. Notes on Computational Fluid Dynamics: General Principles. CFD Direct Ltd, Reading, UK.

Grisogono, B., Belušić, D., 2009. A review of recent advances in understanding the mesoand microscale properties of the severe Bora wind. Tellus A: Dyn. Meteorol. Ocean. 61 (1), 1–16.

He, J., Zhang, H., Zhou, D., Zhou, L., 2025. Spatiotemporal evolution of wind field dynamics and turbulence mechanisms in complex terrain forested areas: A multi-source collaborative observational study. Phys. Fluids 37 (5), 055132.
Heimann, D., 2001. A model-based wind climatology of the eastern Adriatic coast. Meteorol. Z. (Berlin) 10.
Hersbach, H., Bell, B., Berrisford, P., Hirahara, S., Horányi, A., Muñoz-Sabater, J., Nicolas, J., Peubey, C., Radu, R., Schepers, D., et al., 2020. The ERA5 global reanalysis. Q. J. R. Meteorol. Soc. 146 (730), 1999–2049.
Hong, S.Y., Lim, J.O.J., 2006. The WRF single-moment 6-class microphysics scheme (WSM6). Asia-Pacific J. Atmos. Sci. 42 (2), 129–151.
Hong, S.Y., Noh, Y., Dudhia, J., 2006. A new vertical diffusion package with an explicit treatment of entrainment processes. Mon. Weather Rev. 134 (9), 2318–2341.
Huang, M., Liao, S., Lou, W., Lin, W., Kareem, A., 2024. Multi-scale simulation of typhoon wind field at building scale utilizing mesoscale model with nested large eddy simulation. J. Wind Eng. Ind. Aerodyn. 249, 105733.
Huang, C., Yao, J., Fu, B., Calautit, J.K., Zhao, C., Huang, J., Ban, Q., 2023. Sensitivity analysis of WRF-CFD-based downscaling methods for evaluation of urban pedestrian-level wind. Urban Clim. 49, 101569.
Iacono, M.J., Delamere, J.S., Mlawer, E.J., Shephard, M.W., Clough, S.A., Collins, W.D., 2008. Radiative forcing by long-lived greenhouse gases: Calculations with the AER radiative transfer models. J. Geophys. Res.: Atmos. 113 (D13).
Jandaghian, Z., Berardi, U., 2020. Comparing urban canopy models for microclimate simulations in Weather Research and Forecasting Models. Sustain. Cities Soc. 55, 102025.
Janjić, Z.I., 1994. The step-mountain eta coordinate model: Further developments of the convection, viscous sublayer, and turbulence closure schemes. Mon. Weather Rev. 122 (5), 927–945.
Jiménez, P.A., Dudhia, J., González-Rouco, J.F., Navarro, J., Montávez, J.P., García-Bustamante, E., 2012. A revised scheme for the WRF surface layer formulation. Mon. Weather Rev. 140 (3), 898–918.
Kim, D.H., Rho, J.H., Kim, J., 2025. Impact of super high-rise buildings on gust generation in surrounding areas during typhoon landfall: Large-eddy simulations. Sustain. Cities Soc. 131, 106714.
Klemp, J., Durran, D., 1987. Numerical modelling of bora winds. Meteorol. Atmos. Phys. 36 (1), 215–227.
Kozmar, H., Butler, K., Kareem, A., 2012a. Transient cross-wind aerodynamic loads on a generic vehicle due to bora gusts. J. Wind Eng. Ind. Aerodyn. 111, 73–84.
Kozmar, H., Procino, L., Borsani, A., Bartoli, G., 2012b. Sheltering efficiency of wind barriers on bridges. J. Wind Eng. Ind. Aerodyn. 107, 274–284.
Launder, B.E., Spalding, D.B., 1974. The numerical computation of turbulent flows. Comput. Methods Appl. Mech. Engrg. 3 (2), 269–289.
Leal Filho, W., Abeldaño Zuñiga, R.A., Sierra, J., Dinis, M.A.P., Corazza, L., Nagy, G.J., Aina, Y.A., 2024. An assessment of priorities in handling climate change impacts on infrastructures. Sci. Rep. 14 (1), 14147.
Lepri, P., Kozmar, H., Večenaj, Ž., Grisogono, B., 2014. A summertime near-ground velocity profile of the Bora wind. Wind. Struct. 19 (5), 505–522.
Liu, S., Pan, W., Zhao, X., Zhang, H., Cheng, X., Long, Z., Chen, Q., 2018. Influence of surrounding buildings on wind flow around a building predicted by CFD simulations. Build. Environ. 140, 1–10.
Markowski, P., Richardson, Y., 2011. Mesoscale Meteorology in Midlatitudes. John Wiley & Sons.
Mellor, G.L., Yamada, T., 1982. Development of a turbulence closure model for geophysical fluid problems. Rev. Geophys. 20 (4), 851–875.
Metwally, O., Ibrahim, H.A., Elawady, A., Zisis, I., Chowdhury, A.G., 2025. Wind load impact on tall building facades: damage observations during severe wind events and wind tunnel testing. Front. Built Environ. 10–2024.
Miao, Y., Liu, S., Chen, B., Zhang, B., Wang, S., Li, S., 2013. Simulating urban flow and dispersion in Beijing by coupling a CFD model with the WRF model. Adv. Atmos. Sci. 30 (6), 1663–1678.
Mlawer, E.J., Taubman, S.J., Brown, P.D., Iacono, M.J., Clough, S.A., 1997. Radiative transfer for inhomogeneous atmospheres: RRTM, a validated correlated-k model for the longwave. J. Geophys. Res.: Atmos. 102 (D14), 16663–16682.
Mohorovičić, A., 1889. Interessante Wolkenbildung über der Bucht von Buccari (Interesting cloud formation above the Bay of Buccari). Meteorol. Z. 24, 56–58.
Mukul Tewari, N., Tewari, M., Chen, F., Wang, W., Dudhia, J., LeMone, M., Mitchell, K., Ek, M., Gayno, G., Wegiel, J., et al., 2004. Implementation and verification of the unified NOAH land surface model in the WRF model (Formerly Paper Number 17.5). In: Proceedings of the 20th Conference on Weather Analysis and Forecasting/16th Conference on Numerical Weather Prediction, Seattle, WA, USA, vol. 14, pp. 11–15.
Niu, G.Y., Yang, Z.L., Mitchell, K.E., Chen, F., Ek, M.B., Barlage, M., Kumar, A., Manning, K., Niyogi, D., Rosero, E., Tewari, M., Xia, Y., 2011. The community Noah land surface model with multiparameterization options (Noah-MP): 1. Model description and evaluation with local-scale measurements. J. Geophys. Res.: Atmos. 116 (D12).
Nogueira, M., Lima, D.C., Soares, P.M., 2020. An integrated approach to project the future urban climate response: Changes to Lisbon's urban heat island and temperature extremes. Urban Clim. 34, 100683.
Oke, T.R., Mills, G., Christen, A., Voogt, J.A., 2017. Urban Climates. Cambridge University Press.
Park, J.R., Kim, J.H., Shin, Y., Kim, S.H., Chun, H.Y., Jang, W., Tsai, C.L., Lee, G., 2022. A numerical simulation of a strong windstorm event in the Taebaek Mountain Region in Korea during the ICE-POP 2018. Atmos. Res. 272, 106158.
Pastori, S., Mazzucchelli, E.S., 2023. Climate change and extreme wind events: Overview and perspectives for a resilient built environment. In: Wallhagen, M., Cehlin, M. (Eds.), Urban Transition. IntechOpen, Rijeka, p. 177 (Chapter 9).
Pleim, J.E., 2006. A simple, efficient solution of flux–profile relationships in the atmospheric surface layer. J. Appl. Meteorol. Climatol. 45 (2), 341–347.
Pleim, J.E., 2007. A combined local and nonlocal closure model for the atmospheric boundary layer. Part I: Model description and testing. J. Appl. Meteorol. Climatol. 46 (9), 1383–1395.
Pope, S.B., 2013. Turbulent Flows. Taylor & Francis, London.
Potsis, T., Tominaga, Y., Stathopoulos, T., 2023. Computational wind engineering: 30 years of research progress in building structures and environment. J. Wind Eng. Ind. Aerodyn. 234, 105346.
QGIS Development Team, 2024. QGIS Geographic Information System. Technical Report, QGIS Software.
Raicich, F., Malačič, V., Celio, M., Giaiotti, D., Cantoni, C., Colucci, R.R., Čermelj, B., Pucillo, A., 2013. Extreme air-sea interactions in the Gulf of Trieste (North Adriatic) during the strong Bora event in winter 2012. J. Geophys. Res.: Ocean. 118 (10), 5238–5250.
Repetto, M.P., Burlando, M., Solari, G., De Gaetano, P., Pizzo, M., Tizzi, M., 2018. A web-based GIS platform for the safe management and risk assessment of complex structural and infrastructural systems exposed to wind. Adv. Eng. Softw. 117, 29–45, Special Section - CIVIL-COMP 2017.
Ricci, A., Burlando, M., Repetto, M., Blocken, B., 2022. Static downscaling of mesoscale wind conditions into an urban canopy layer by a CFD microscale model. Build. Environ. 225, 109626.
Richards, P.J., Hoxey, R.P., 1993. Appropriate boundary conditions for computational wind engineering models using the k-ε turbulence model. J. Wind Eng. Ind. Aerodyn. 46–47, 145–153, Proceedings of the 1st International on Computational Wind Engineering.
Richards, P., Norris, S., 2011. Appropriate boundary conditions for computational wind engineering models revisited. J. Wind Eng. Ind. Aerodyn. 99 (4), 257–266, The Fifth International Symposium on Computational Wind Engineering.
Roache, P.J., 1994. Perspective: A method for uniform reporting of grid refinement studies. J. Fluids Eng.-Trans. ASME 116 (3).
Roache, P.J., 1997. Quantification of uncertainty in computational fluid dynamics. Annu. Rev. Fluid Mech. 29 (1), 123–160.

Seneviratne, S.I., Zhang, X., Adnan, M., Badi, W., Dereczynski, C., Luca, A.D., Ghosh, S., Iskandar, I., Kossin, J., Lewis, S., Otto, F., Pinto, I., Satoh, M., Vicente-Serrano, S.M., Wehner, M., Zhou, B., 2021. In: Masson-Delmotte, V., Zhai, P., Pirani, A., Connors, S.L., Péan, C., Berger, S., Caud, N., Chen, Y., Goldfarb, L., Gomis, M.I., Huang, M., Leitzell, K., Lonnoy, E., Matthews, J.B.R., Maycock, T.K., Waterfield, T., Yelekçi, O., Yu, R., Zhou, B. (Eds.), Climate Change 2021: The Physical Science Basis. Contribution of Working Group I to the Sixth Assessment Report of the Intergovernmental Panel on Climate Change. Cambridge University Press, Cambridge, United Kingdom and New York, NY, USA, pp. 1513–1766 (Chapter Weather and Climate Extreme Events in a Changing Climate).

Skamarock, W.C., Klemp, J.B., Dudhia, J., Gill, D.O., Liu, Z., Berner, J., Wang, W., Powers, J.G., Duda, M.G., Barker, D.M., et al., 2019. A description of the advanced research WRF version 4. NCAR Tech. Note ncar/tn-556+ str 145.

Smith, R.B., 1987. Aerial observations of the Yugoslavian bora. J. Atmos. Sci. 44 (2), 269–297.

Tewari, M., Kusaka, H., Chen, F., Coirier, W.J., Kim, S., Wyszogrodzki, A.A., Warner, T.T., 2010. Impact of coupling a microscale computational fluid dynamics model with a mesoscale model on urban scale contaminant transport and dispersion. Atmos. Res. 96 (4), 656–664.

Thompson, G., Field, P.R., Rasmussen, R.M., Hall, W.D., 2008. Explicit forecasts of winter precipitation using an improved bulk microphysics scheme. Part II: Implementation of a new snow parameterization. Mon. Weather Rev. 136 (12), 5095–5115.

Tominaga, Y., Mochida, A., Yoshie, R., Kataoka, H., Nozu, T., Yoshikawa, M., Shirasawa, T., 2008. AIJ guidelines for practical applications of CFD to pedestrian wind environment around buildings. J. Wind Eng. Ind. Aerodyn. 96 (10), 1749–1761, 4th International Symposium on Computational Wind Engineering (CWE2006).

Toparlar, Y., Blocken, B., Maiheu, B., van Heijst, G., 2017. A review on the CFD analysis of urban microclimate. Renew. Sustain. Energy Rev. 80, 1613–1640.

UN, 2020. The Human Cost of Disasters: An Overview of the Last 20 Years (2000–2019). UN Office for Disaster Risk Reduction Geneva, Switzerland, UN Office for Disaster Risk Reduction.

Večenaj, Ž., Belušić, D., Grisogono, B., 2010. Characteristics of the near-surface turbulence during a bora event. Ann. Geophys. 28 (1), 155–163.

Wang, L., Mačak, M.B., Stanič, S., Patruno, L., Dong, W., Chen, D., 2025. Orography-induced atmospheric small-scale waves during Bora using lidar observations and numerical simulations. Geophys. Res. Lett. 52 (4), e2024GL112400.

Wieringa, J., 1992. Updating the Davenport roughness classification. J. Wind Eng. Ind. Aerodyn. 41 (1), 357–368.

Yamada, T., Koike, K., 2011. Downscaling mesoscale meteorological models for computational wind engineering applications. J. Wind Eng. Ind. Aerodyn. 99 (4), 199–216, The Fifth International Symposium on Computational Wind Engineering.

Yang, D., Zhang, N., Tang, J., 2025. Impacts of urban morphology on typhoon-induced wind hazards at the pedestrian level. Urban Clim. 60, 102351.

Yue, H., Guo, P., Zhao, Y., Ning, X., Zhou, L., Zhang, H., 2024. Numerical reconstruction of atmospheric boundary layer seasonal turbulent wind field over a complex forest terrain. Phys. Fluids 36 (10), 105174.

Zhao, Z., Xiao, Y., Li, C., Chan, P.W., Hu, G., Zhou, Q., 2023. Multiscale simulation of the urban wind environment under typhoon weather conditions. Build. Simul. 16 (9), 1713–1734.

Zheng, Y., Miao, Y., Liu, S., Chen, B., Zheng, H., Wang, S., 2015. Simulating flow and dispersion by using WRF-CFD coupled model in a built-up area of Shenyang, China. Adv. Meteorol. 2015 (1), 528618.

Zheng, S., Wang, Y., (John) Zhai, Z., Xue, Y., Duanmu, L., 2021. Characteristics of wind flow around a target building with different surrounding building layers predicted by CFD simulation. Build. Environ. 201, 107962.

Zonato, A., Martilli, A., Jimenez, P.A., Dudhia, J., Zardi, D., Giovannini, L., 2022. A new $k-\varepsilon$ turbulence parameterization for mesoscale meteorological models. Mon. Weather Rev. 150 (8), 2157–2174.